THE UTILISATION OF COMMERCIAL OFF THE SHELF CARBON NANOTUBE FIBRE IN INDIVIDUAL METAMATERIAL ANTENNAS TO ENABLE A REDUCTION IN OPERATING FREQUENCIES

MR ANDREW KING

Submitted in Partial Fulfilment of the Requirements of an M.Sc by Research, July 2019.

The page intentionally left blank

Contents

List of Abbreviations

SWCNT	Single-walled carbon nanotubes
COTS	Commercial off the shelf
SRR	Split ring resonator
LC	Inductance capacitance
NF	Nanotube fibre
RBM	radial breathing mode
HFSS	High Frequency Structure Simulator
OD	Outer diameter
RAM	Radar absorbent material
DOS	Density of States
ARPES	Angle-resolved photoemission spectroscopy

List of Figures

List of Tables

List of Equations

Acknowledgements

I wish to express my profound gratitude to my main supervisor Dr John E Proctor and my co-supervisor Dr Dan Bull for their guidance during the course of the entire research work. Dr Proctor has been supportive and has given me freedom to pursue various aspects of the project without objection, also provide understanding discussion about the nanomaterials aspect of the research.

My appreciation goes to my colleagues at QinetiQ for their support towards providing facilities, time, financial support and expertise throughout the course of this research work.

This dissertation writing would not be complete if I failed to express my gratitude to the school of Computing, Science and Engineering, University of Salford, Manchester for their support and encouragement throughout my studies.

Abstract

In this project it is investigated whether the utilisation of commercial off the shelf carbon nanotube fibre in antenna designs created as part of metamaterial research, can be used to produce electrically small antennas

We find that basic improvements to metamaterial antenna designs enable low broadcast frequencies utilising standard bulk metals. However, the increased surface area of the carbon nanotube fibre enables further reductions in frequency. From these results we find that carbon nanotube fibre metamaterial antennas may provide attractive alternatives to existing electrically-small antennas.

This page intentionally left blank

Introduction

1. Conventional antennas have a length (L) at least ¼ of the wavelength, λ, at which they transmit and receive. However, it was proposed in 1999 [1] that a completely different approach could be taken to antenna design – utilizing an array of conductive parasitic structures with dimensions significantly smaller than the wavelength of the incident or transmitted electromagnetic waves. These materials have been labelled "metamaterials" and enable an efficient, highly directional, antenna.
2. Whilst metamaterials have been developed making use of conventional metals such as copper, recent advances in the synthesis of single-walled carbon nanotubes (SWCNTs) present these materials as a potentially far better material from which to construct metamaterials.
3. First successfully synthesized in 1993 [2], SWCNTs consist of an individual sheet of graphene rolled up on itself to form a tube. Their theoretical electrical conductivity is extremely high compared to materials generally regarded as good electrical conductors (copper, gold etc.). Since 1993 synthesis methods for SWCNTs have been improved to the point where SWCNTs and fibres comprising bundles of SWCNTs, are commercially available at sufficiently low prices to make their widespread usage economical.
4. In this dissertation commercial off the shelf (COTS) CNT fibre, alongside copper is utilised to construct a specific kind of metamaterial antenna comprising nested split rings. These types of metamaterial antennas, usually comprising thin copper plates, both individually and in an array have been shown to enable electrically efficient low frequency broadcast/radiation from physically small sizes. Design improvements to the original split ring antenna components, alongside the geometric properties of the CNT fibre, are shown to enable a significant decrease in efficient broadcast frequencies.
5. The dissertation is broken down into three chapters. In chapter 1, a short history of split ring resonators, alongside any design improvements enabling a decrease in the broadcast frequencies are indicated from published literature. Further to this, a qualitative analysis and explanations as to why these design improvements are important are indicated. A subsequent section contains a review of papers, and publications detailing exactly what carbon nanotubes are, how they are classified, and how their electrical conductivity properties relate to these classifications. Reviews of both Raman spectroscopy, the sole method of CNT characterisation utilised within the project, and methods of CNT fibre creation are contained in order to end the chapter.
6. The second chapter contains the methodology utilised in the dissertation to predict, analyse and model the split ring antennas. Electrical conductivity measurements of the CNT fibre, followed by Raman spectroscopy are utilised to characterise the physical materials used in the project. Further, computational modelling is used throughout in an attempt to apply and predict the behaviour of the design decisions contained within the first chapter. This chapter concludes with prototype antenna build and transmission loss measurements, and the results are analysed, and compared to the previous modelling work.
7. The final chapter contains a discussion of the performance and efficiencies of the experimental CNT fibre and copper ring prototypes, indications of any potential draw backs to commercial usage and recommendations for any future follow-up work.

This page intentionally left blank

Chapter 1: Literature Review & Theory

8. Introduction

9. As a full overview of current and historic split ring resonator (SRR) development and their related usage in antennas (metamaterial and otherwise) are beyond the scope of this dissertation, the first part of this literature review provides a brief review of any literature which include design decisions which enable the design of smaller, more efficient antennas. Following this, in an associated sub-section, a theoretical explanation is attempted in order to explain the design criteria referenced from the publications, and further to how these criteria may be modified to allow even lower resonant frequencies for the SRRs. Likewise, a further part of the review looks at the production techniques of both carbon nanotubes and the associated fibres.

10. Split Ring Resonators

11. The information contained within this section is wholly qualitative. For the interested reader, a basic mathematical overview of the operation of split ring resonators is contained within Appendix 1

12. Split ring resonators are first referenced in [1]. The paper was presented in order to show the theoretical creation of materials with negative magnetic permeabilities ($\mu_{eff} < 0$). A mathematical treatment of a material with $-\mu_{eff}$ was first theorised by Veselago, in 1968 [3] have sizes much smaller than the wavelength of any incident radiation. Were the structures of to be a similar or larger size than the wavelength of this radiation, the possibility exists that any theoretical or experimental results indicating a $-\mu_{eff}$ could be caused by the internal structure of these types of elements diffracting or refracting the radiation. The structures comprise a nested ring configuration (one ring inside the other, effectively two thin hollow plates) where, under an externally induced electrical load, a capacitance is introduced into the structure across the volume between the two rings. Further to this, a single split per ring is introduced into the opposite sides of each ring. This not only prevents current from flowing around each ring, but also causes a displacement current to flow between the rings, further enhancing any capacitive effect.

13. The basic unit cells comprising a double, thin, hollow plate structure, created in [1] are easily packed into arrays. They are designed as such with a need to disable the continuous electrical path provided along the shaft of a cylindrical structure, as any significant induced current travelling normal to the plane the structure resides in will severely interfere with any magnetic resonance otherwise created by the displacement current between the rings.

14. Materials therefore, comprising numerous microstructures containing split rings can be designed as required with considerable magnetic activity, both diamagnetic and paramagnetic, and can if desired be made extremely light [1]. The geometric properties of the structure created in [1] are contained within the figure below.

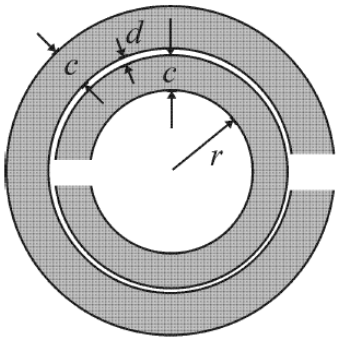

15. *Figure (1). A plan view of a split ring structure, where c = 0.9 mm, d = 0.2 mm, r = 3.6 mm, and the gap width (not shown on the diagram) = 0.2 mm.* [1]

16. The topology of a split ring resonator shown in Figure (1) is referred to as the standard SRR configuration for the rest of the dissertation.

17. As the work in [1] was conducted in the microwave domain, it was quickly theorised that materials comprising an array of these microstructures could be utilised as small antennas, i.e. antennas able to operate somewhat efficiently at wavelengths much larger than the physical size of the antenna.

18. The fundamental limits of small antennas were initially devised by Harold Wheeler in 1947 [4]. These are characterised as showing low radiation resistance, high reactance and narrow bandwidths. A year later Chu alongside Wheeler [5] defined a small antenna as an antenna that can fit inside a sphere whose diameter is $\frac{1}{\pi}\lambda$.

19. Successfully utilising individual SRRs as parasitic elements coupled to small monopole antennas, reference [6] shows that resonant frequencies seen in the infinite array approach, as seen in [1], can be replicated by individual SRRs.

20. Modifying the geometric properties of ring structures via differing numbers of splits and rings are investigated both numerically and experimentally in [7] and [8]. Decreases in the resonance frequencies of standard configuration outer diameter structures are shown in an individual-ringed SRR by the addition of a second ring, likewise the addition of extra splits into one or multiple rings will increase the resonance frequency, but increase the directivity of the device. The authors make note that the orientation of the splits are important, with a symmetric split orientation (splits in each ring at opposite sides to each other) providing the lowest resonance frequencies, and increased efficiencies.

21. Further modification to the parameters of a standard configuration SRR, [8], shows that as the split and gap widths are increased, the resonant frequency (ω_m) increases. Likewise, the addition of external capacitors show a marginal decrease in the bandwidth available from the structures. Previously developed analytical models of SRRs [9] also predict the same behaviour, while also noting an increase in the metal width of the rings (as opposed to the height from the substrate), while keeping the gap/split widths constant will increase the resonant frequency. The addition to the standard configuration SRR with the addition of surface mounted capacitors will reduce the resonant frequency but have the undesirable effect of reducing the efficiency of the structures, where the efficiency in this paper is defined as the ability of an antenna to absorb power.

22. An increase in ring height shows a decrease in resonant frequency [11] (where the ring height is defined as the height of the ring from the substrate), however no reduction in efficiency is seen. Likewise, also shown in [11], the resonant frequency of an SRR will decrease as the value of ε_r in the substrate increases.

23. A simple model developed by Baena, Marques and Medina [12], models an SRR element as an inductance capacitance (LC) circuit. The authors state the assumption that an SRR unit

cell of a much smaller size than the free space wavelength will behave as a quasi-static LC circuit.

24. SRR design conclusions and theory

25. From the literature reviewed so far, we can draw certain design criteria, which when applied to an individual antenna comprising split rings should enable efficient low frequency broadcast. In this sub-section each criterion is stated and a theoretical explanation (if possible) is given.

26. *Split and gap distances should be reduced to as low as manufacturing capabilities allow*.

27. Treating an SRR as a quasi-static LC circuit, where such circuits depend on the storage of energy in both the electric and magnetic fields, and the oscillation of energy between the two storage media, the resonant frequency f_0 is given by;

$$f_0 = \frac{1}{2\pi\sqrt{LC}}$$

28. *Equation (1): The resonant frequency of an LC circuit (in Hz), where L and C are the inductance and capacitance respectively.*

29. Looking at the individual equations relating to capacitance and inductance we can see how they relate to the criterion stated above, and further to this we can explain the second criterion;

30. *Substrate relative permittivity (ε_r) should be as high as possible.*

31. Utilising the equation for a parallel plate capacitor;

$$C = \varepsilon_r \frac{A}{d}$$

32. *Equation (2): The capacitance between two parallel plate capacitors, where C is the capacitance in farads, ε_r is the relative permittivity, A is the area of overlap in m^2, and d is the separation distance between the plates.*

33. As d is decreased, and ε_r is increased the overall capacitance (C) will be increased. The majority of the results presented in the literature utilise the standard SRR configuration, with wide, flat plates for the conducting elements (0.9 mm ring widths x 0.03 mm thickness). From this we can approximate the faces of each individual ring facing the other as parallel plates. If we ignore any edge effects we can presume that any electric field lines created as part of any capacitive effects head straight across the gap between each plate, and decrease in magnitude as a function of distance, or as a function of the dielectric medium loss tangent ($\tan \delta_c$). Any reduction in the separation distance (d) (for both the split and width distances) in any SRR element to the minimum value possible should reduce energy storage losses. Likewise, increasing the relative permittivity of the dielectric medium (ε_r) should enable a greater capability within a capacitor to store energy and therefore provide a larger capacitance.

34. As the capacitance and inductance of an SRR system are inherently linked to the resonant frequency of the system, a similar increase in the inductance will enable a further a further reduction in resonance frequency.

35. Further to this, increasing the relative permeability (μ_r) will provide an increase in the inductance, as can be seen in equation 3;

$$L = \frac{\mu_r N^2 A}{l}$$

36. *Equation (3): Inductance of a solenoid, where L is the inductance in Henrys, μ_r is the relative permeability (in Henries/meter), N is the number of turns in the solenoid, A is the cross-sectional area of the solenoid (in m)^2, and l is the length of the wire (in m).*

37. An analytical expression to determine the resonant frequency of a flat plate SRR is given in equation 19, in Appendix 1.

38. Treating an SRR as a solenoid with only 1 turn (N = 1) and a wire length less than the circumference, we can increase the inductance by increasing the cross-sectional area, A, or by increasing the value of μ_r. Once again, we run into the problem of decreasing magnetic field strength as a function of distance, i.e. a large diameter solenoid will inevitably have a lower magnetic field strength in its centre compared to a smaller solenoid of an equal number of turns. As such we can increase the inductance of a solenoid (or SRR in this case) by increasing the capability of the dielectric near to or in the interior of the solenoid to store energy. This can be done by finding a dielectric with an appropriately large μ_r.

39. *The SRRs should comprise a minimum of 2 rings.*

40. While individual split ring resonators have been shown [7], the introduction of a second (or more) ring enables greater capacitance values, which come from the area of overlap of both plates and the volume enclosed between each ring.

41. *The Ring thickness should be as thin as possible.*

42. In any electrical circuit, any wire, or conductive medium will exhibit a self-inductance which is a function of the relative permeability and, geometric properties of the wire and wire thickness. In general, in electronic circuits, any inductance at specific frequencies may lead to unwanted effects such as increased signal attenuation.

$$L_{wire}(L, D) = 2L\left\{ln\left[\left(\frac{2L}{D}\right)\left(1+\sqrt{1+\left(\frac{D}{2L}\right)^2}\right)\right]-\sqrt{1+\left(\frac{D}{2L}\right)^2}+\frac{\mu_r}{4}+\left(\frac{D}{2L}\right)\right\}$$

43. *Equation (4): The inductance of a straight wire (in Henries [H]), where D is the diameter of the wire (m), L is the length of the wire (L), and μ_r is the relative permeability of the wire.* [13]

44. We can see from equation 4, however, that decreasing the thickness of the wires in an SRR, will increase the self-inductance of the wire, which in turn will lead to an increase in the overall inductance of the entire system and thereby support lower resonance frequencies.

45. *Substrate thickness should be as thick as possible.*

46. The electrical field associated with an SRR will be primarily (if not solely) based in the dielectric volumes contained wholly within the split and gaps in an SRR. The magnetic field however, much as we would see in a solenoid (or bar magnet), is expected to encompass a volume much larger than the SRR itself. If then, this volume, or as much as is practicable,

can be utilised to increase energy storage, less energy should be lost to the surrounding environment. This then will dictate that any substrate the SRR sits on (or in) should be as large as possible.

47. *Substrate transmission loss (tan δ_c) should be as low as possible.*

48. There is one caveat to the substrate thickness criterion mentioned above. Any substrate by its very nature will not be as conductive as the materials used in the antenna elements in the system, and may act to attenuate incoming RF/microwave radiation. This will tend to increase any transmission losses through the substrate to the antenna elements. The materials used for the substrate should therefore have as low a transmission loss as possible, or the thickness and diameter of any substrate with a high transmission loss should be balanced against the inherent permeability of the material. This also means that a substrate should not be placed in between the expected radiation source and the antenna element, as energy may be lost to the substrate before it reaches the antenna itself.

49. Carbon Nanotubes

50. Carbon nanotubes (CNTs) are, alongside graphene, allotropes of carbon. They are cylindrical nanostructures, with diameters of 0.7 nm – 2.0 nm for typical SWCNTs. While, in a basic sense, two different forms of CNT exist, single walled carbon nanotubes (SWCNT) and multi-walled carbon nanotubes (MWCNT), the primary focus of this project is on SWCNTs due to the expected improved electrical conduction properties they display compared to their multi-walled relations. However, MWCNTs shall be touched upon in this review if only to help clarify the history of CNTs, explain their properties and enable correct identification of SWCNTs from the analysis techniques utilised.

51. The discovery of Buckminsterfullerenes (C_{60}), formed via pulse laser ablation of graphite by Kroto et al. in 1985 [14], lead to a hypothesis by Saito et al [15] that an extremely small diameter carbon fibre could be created in which a single pristine layer of graphite (graphene) could extend all the way around the fibre's circumference and join back on itself.

52. Using a laser ablation method similar to the method used by Kroto et al. the synthesis of the first MWCNT is credited to Ijima in 1991 [16]. However, MWCNTs may have been synthesised many decades prior in the Soviet Union, with the earliest paper from 1952, by Radushkevich and Lukyanovich. [17] The authors identified what are now known as MWCNT via the use of transmission electron microscopy, which is still the most direct method of determining the number of nanotube, or graphite walls/layers.

53. SWCNTs were discovered by two groups independently of each other. Bethune and co-workers at IBM in the United States, and Iijima and Ichihashi at NEC corporation in Japan. Both discoveries were published in Nature in 1993 [18].

54. A SWCNT as one might expect, is formed from a single continuous sheet of graphene rolled up and joined in on itself. The tubes are usually, although not always, capped off by a semi spherical fullerene molecule. The smallest of these "capped" SWCNTs have the ends capped by the smallest diameter fullerene molecules with a diameter of 0.7 nm [19], with larger "capped" SWCNTs capped by larger molecules.

55. SWCNTs can be characterised [20] by their chiral vector (**C**h). Where, other than their length, SWCNTs can be completely described by this vector. The vector stretches between any two carbon atoms chosen in a graphene sheet, and is defined by the relation;

$$\mathbf{C}h = n\mathbf{a}_1 + m\mathbf{a}_2$$

56. *Equation (5): The chiral vector of a Carbon nanotube, where n and m are integers, and a1 and a2 are the unit cell vectors of the two-dimensional lattice formed by the graphene sheets.*

57. The direction of the nanotube axis is perpendicular to this chiral vector.

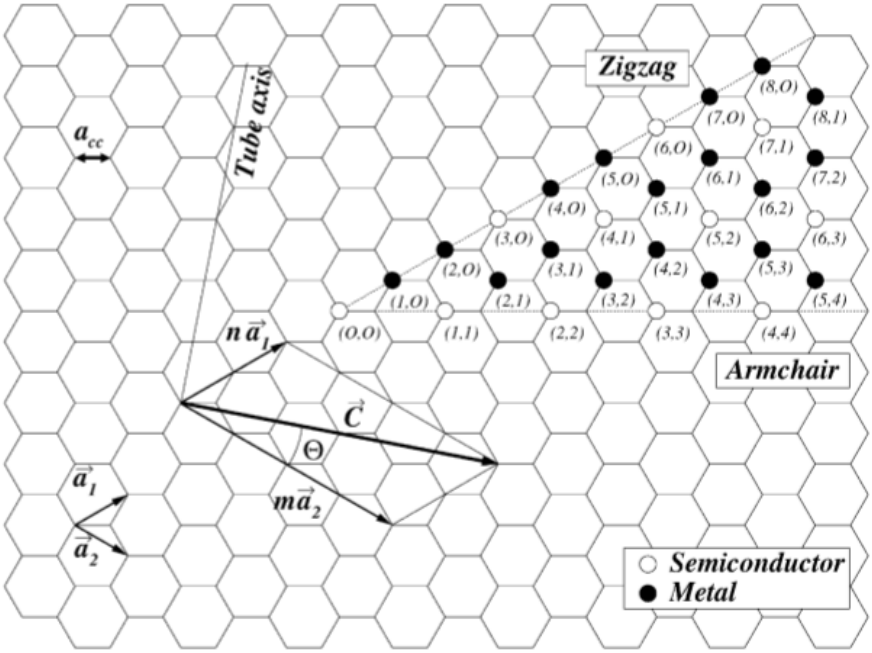

58. *Figure (2): Chiral vector C and chiral angle Θ definition for a (2, 4) nanotube on graphene sheet. a_1 and a_2 are the unit cell vectors of the two-dimensional hexagonal graphene sheet. The circumference of nanotube is given by the length of chiral vector. The chiral angle Θ is defined as the angle between chiral vector **C**h and the zigzag axis.* [20]

59. The circumference of a SWCNT is given by the magnitude of the chiral vector **C**h. The corresponding relationship relates the chiral vector **C**h and the circumference;

$$c = \boldsymbol{C}h = \boldsymbol{a}\sqrt{(n^2 + nm + m^2)}$$

60. *Equation (6): The relationship between the Chiral vector (**C**h), and the circumference of a carbon nanotube, **w**here the value **a**, is the length of the unit cell vector $\mathbf{a}_1$ or $\mathbf{a}_2$.*

61. This length **a** is related to the carbon-carbon bond length a_{cc} by the relation;

$$a = |\boldsymbol{a}_{1|}| = |\boldsymbol{a}_2| = a_{cc}\sqrt{3}$$

62. *Equation (7): The relation between the carbon-carbon bond length and length of the unit cell a.*

63. While the carbon-carbon length is a_{cc} = 0.142 nm, and that the same figure is often used for nanotubes [21] a slightly larger value of a_{cc} = 0.144 nm could be a better approximation due to the curvature of a tube. [22]

64. From Figure 2, the chiral angle, i.e. the angle between the zigzag nanotube axis and the chiral vector **C**h, is given by;

$$\Theta = tan^{-1}\left(\frac{m\sqrt{3}}{m+2n}\right)$$

65. *Equation (8): The chiral angle for a carbon nanotube.*

66. Nanotubes can be described solely by a pair of integers (n,m), which are related to their chiral vector. They then define three types of nanotubes. When n = m, the nanotube is defined as an armchair type ($\theta = 0^0$). When m = 0, then the nanotube is defined as the zigzag type ($\theta = 30^0$). Otherwise, when $n \neq m$, the nanotube is defined as a chiral tube, and θ takes a value between 0° and 30°. The value of (n,m) then determines the chirality of the nanotube, which in turn effects the optical, mechanical and electronic properties. Where [23] states that Nanotubes with |n − m| = 3q are metallic and those with |n − m| = 3q ± 1 are semiconducting (q is an integer)."

67. The above assumption comes from an expected crossing of the valence and conduction bands at the Fermi energy level, implying that the CNT is metallic, otherwise it is expected to be a semiconductor. The bandgap for metallic nanotubes while expected to be zero, has been observed by Lieber et al. in zigzag metallic SWCNTs to be as low as 0.029 eV for (15,0) [24].

68. The question then needs to be asked as to what conductivity would one expect for a pure SWCNT, i.e. one without any dopants, defects or impurities ? From the theoretical calculations contained within [25], we can evaluate the group velocity, **v**(k), of electrons at the Fermi level (i.e. the K point). With the dispersion relation being linear, the group velocity is a constant **v**(k) = v_f = 1.0 x 10^6 ms^{-1}.

69. Of interest to note from [25] is that, at the K point, the relationship between electron energy and their associated wavevector is linear. This is normally the case for massless particles, i.e. photons, where we write E = ($\hbar$kc), while for particles with non-zero effective masses we would usually write E = ($\hbar^2k^2/2m^*$).

70. Results from [26], in which the electron dispersion relation was directly measured by an ARPES (Angle-resolved photoemission spectroscopy) experiment on graphene, show that the theoretical calculations as indicated in [25] are remarkably accurate, and that the electrons in a pure sample of graphene move a relativistic velocity close to vf ≈ 1.0 x 10^6 ms^{-1}.

71. Over a small enough path length, electrons in all conductors and insulators under an induced EMF would be expected to move at the Fermi velocity inherent to the particular materials. What makes graphene (and CNTs) special in comparison with other materials are the differences between the Fermi velocities and the measured, or drift velocities. The dispersion relation near the Fermi level of copper can be calculated to be $\mathbf{v}_f \approx 2.8 \times 10^5$ ms^{-1} [27], likewise in Tungsten $\mathbf{v}_f \approx 4 - 5 \times 10^5$ ms^{-1} [28], but the drift velocity in these metals is ~1 mm s^{-1}. This difference in drift velocity compared to the Fermi velocity can be explained by both the thermal motion of ions and scattering via defects in the metal lattice thus causing the electron motion to be diffusive rather than ballistic. The ballistic velocity in this sense from [25] is defined as a charge conductor in a medium obtaining and maintaining a quantum state with a given wave vector. A diffusive velocity is then defined as the electrons being regularly scattered into different quantum states by defects, or by thermal motion of the surrounding ions. The lack of large concentrations of defects in a metallic SWCNT, or graphene lattice, will allow the electrons (at ambient temperatures) to have ballistic and therefore Fermi velocities.

72. Raman spectroscopy of Carbon Nanotubes

73. As the performance of an antenna is expected to be largely dependent on the electrical conductivity of the material utilised as the conducting element, the four-point method will be utilised in the materials analysis section to determine the electrical conductivity of the CNT fibre sample used in prototype production (more on this in the relevant section). Following from this, and in order to help explain these measurements and characterise the composition of the CNT fibre, Raman spectroscopy is used in order to determine the diameter and chirality comprising the fibre. This sub-section therefore gives a brief overview of the technique.

74. The Raman spectra of graphene and CNTs, can enable the identification of the 1-dimensional properties of these materials [29]. As a technique it is well suited to give information about their phonon and electronic structures. Likewise, as the mechanical, thermal, electrical and elastic properties in both graphene and CNTs are strongly influenced by the phonons and phonon movement in the material lattice, it can be used to support theoretical predictions about these materials.

75. A Raman experiment is relatively simple, with readily available equipment. It can be performed at room temperature, under ambient pressure, is none destructive, and none invasive. These properties make it particularly well suited compared to other techniques of graphene or CNT characterisation.

76. While Raman spectra usually only involve phonons, the scattering efficiency of the technique gets larger when the laser energy matches the energy difference between the conduction and valence bands of the materials. The resonant Raman intensity depends on the electronic density of states (DOS) available for these transitions. This is a particularly important for 1-dimensional systems.

77. The DOS in 1-dimensional systems are characterised by van-Hove singularities. Sharp singularities in these systems define narrow energy ranges where the density of states become very large.

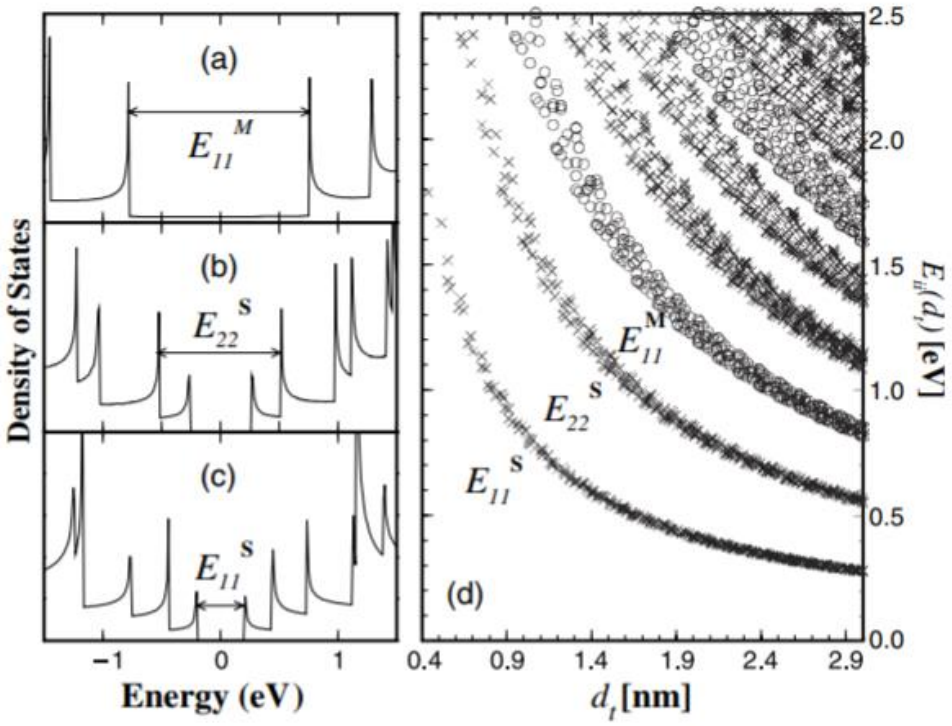

78. *Figure (3): DOS for a (a) armchair (10, 10) SWCNT, (b) chiral (11, 9) SWCNT and (c) zigzag (22, 0) SWCNT obtained with the tight binding model displayed in (d) [62]. Shows the electronic transition energies Eii for all the (n, m) SWCNTs with diameters from 0.4 to 3.0 nm using a simple first-neighbour tight binding model. Distortion from this simple one-electron model is expected for the lower energy transitions ES 11 and for SWCNTs with dt < 1 nm. [29]*

79. In practice, this means that in bundles of SWCNTs, only the SWCNTs with energies in resonance with the incident laser spectra will contribute strongly to the spectrum.

80. Figure 3 (d) is termed a Kataura plot [30], where each point in the plot represents one optically allowed electronic transition energy (E_{ii}) from a SWCNT with a given chirality (n,m). Crosses come from semiconducting SWCNTs and circles from metallic SWCNTs. A Kataura plot can be reference against all CNT (n,m) assignments, and any CNTs in a sample will be in resonance with a particular incident laser energy used to excite a sample. Further, these types of plots can be utilised to determine the metallic and semi-conducting make-up of the SWCNTs, thereby helping to explain any electrical, thermal or mechanical properties. It is expected, however, that any none resonant scattering will be "drowned" out by the signal from the resonant processes and, as such, a wide variety of laser wavelengths should be employed to gather as much data as possible

81. The figure from [29], showing the primary Raman features from a sample of SWCNT bundles is shown below.

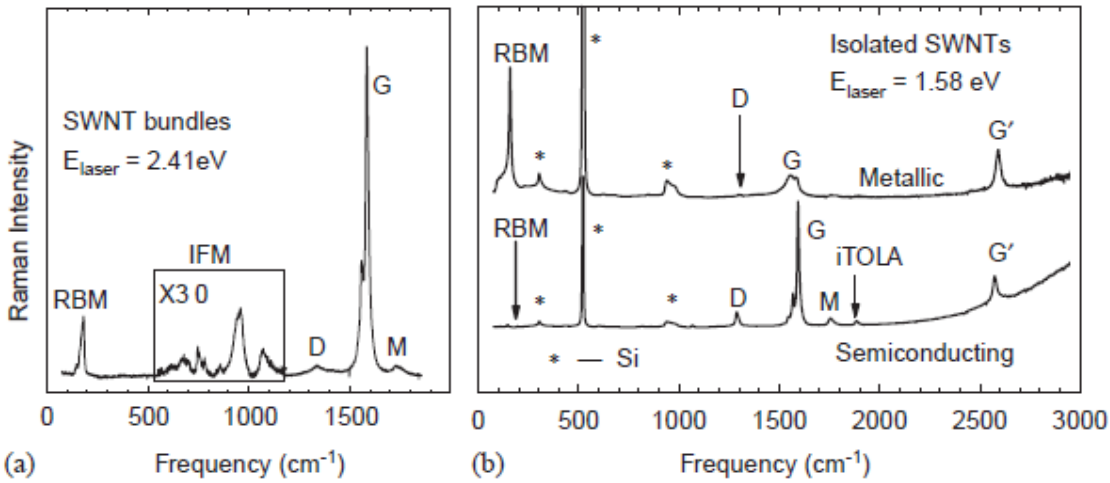

82. *Figure (4). (a) Raman spectra from HiPco SWCNT bundles, (b) Raman spectra from a metallic (top) and a semiconducting (bottom) SWCNT at the single nanotube level. The spectra show the radial breathing modes (RBM), D-band, G-band and G'band features, in addition to weak double resonance features associated with the M-band and the iTOLA second-order modes, where the iTOLA modes are a combination of optical and acoustic modes. The isolated carbon nanotubes are sitting on an oxidized silicon (Si) substrate which provides contributions to the Raman spectra denoted by "*", and these Si features are used for calibration purposes.* [290]

83. The two dominant features that can be seen in the SWCNT (denoted as SWCNT in the figure above) are the radial breathing mode (RBM) and the G peak.

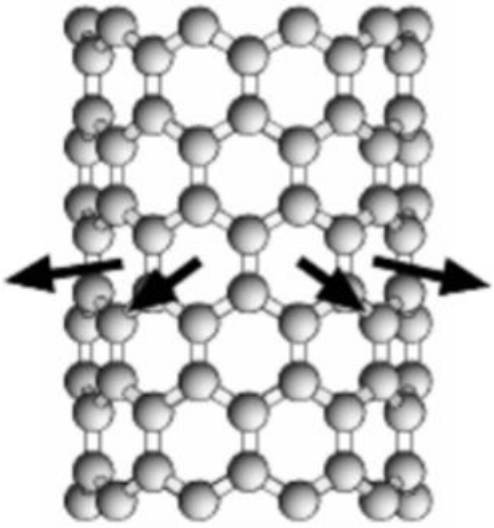

84. *Figure (5): SWCNT RBM of the carbon atoms in the lattice.* [29]

85. The Radial breathing mode (RBM) of an SWCNT is indicative of an expansion and contraction of the entire tube under the influence of an external pressure or energy source. If we use a ball on a string model, the RBM frequency(ω) of an individual SWCNT will be inversely proportional to the SWCNT diameter d_t.

$$\omega_i(d_t) = \frac{A}{d_t} + B$$

86. *Equation (9): The RBM frequency (ω_i) as a function of nanotube diameter (d_t)*

87. Where A has an approximate value of 234 nm.cm^{-1} and has been determined from first principles (ab initio) calculations. B is approximately 10 cm^{-1}, which corrects for intertube interaction frequencies in SWCNT bundles. [31]

88. Experimental measurements on individual SWCNTs tend to agree with this relation [25]. Occasionally, $\omega_i(d_t)$ show different values from measurement. In these cases, the frequencies are always higher than we would expect. Higher frequencies indicate an increased resistance to expansion from the environment against the SWCNT, and therefore a higher restoring force, and in a classical sense a higher spring constant.

89. From this external restoring force, [25] indicate a further two different $\omega_i(d_t)$ relations have been found to provide good fits to different sets of experimental data.

$$\omega(d_t) = \frac{A'}{d_t}\sqrt{1 + Cd_t^2} = \omega + \frac{A'}{d_t}\left[\sqrt{1 + Cd_t^2} - 1\right]$$

90. *Equation (10): Relationships between RBM frequency and nanotube diameters when the nanotubes are under the influence of an external restoring force.*

91. The tubes in this case show a more complex model of SWCNTs vibrating under external pressures.

92. Alongside the RBM peak(s), the G peak can be used to support analysis of any Raman results. The G peak in SWCNTs are split into multiple peaks, while in graphene and graphite a single Lorentzian peak at ca. 1580 cm^{-1} would be seen. Of note with regards to this peak is that it comes from a single resonant Raman-scattering process.

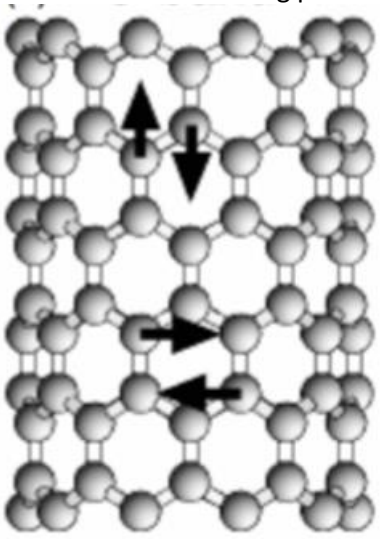

93. *Figure (6): Motion of the carbon atoms related to the G band. Top arrows are LO, and bottom arrows are TO. [31]*

94. The G peak corresponds to a vibration of atoms out of phase along the same axis. The energy of the vibration in SWCNTs depends on the angle of vibration in relation to the tube axis. The phonon wavevector is quantized in the direction around the circumference of the SWCNT, which causes splitting in the allowed phonon modes at the Γ point.

95. The G peak observed experimentally in a Raman spectrum of SWCNTs comprise G+ and G- peaks at high and low frequencies respectively. These correspond to atomic displacements in-plane along the tube axis (LO), or perpendicular to the tube axis (TO), where TO corresponds to the G+ peak and LO to the G- peak, or vice versa depending on the metallic/semiconducting nature and chirality of the SWNCT observed.

96. The separation distance between the G+ and G- peaks increases as the diameter of the tube decreases, likewise the line shape and relative intensity of the G+ and G- peaks vary strongly according to the exact (n,m) assignment. All armchair (n,n) SWCNTs exhibit only a narrow G+ peak [32],while all zigzag (n,0) SWCNTs exhibit a sole peak, a broad G- peak in metallic zigzag tubes and a narrow G+ peak in semiconducting tubes. None armchair metallic SWCNTs exhibit both peaks, but the G- peak shows a highly asymmetric Breit-Wigner-Fano line shape instead of the usual Lorentzian [32].

97. While the CNT fibre utilised in this dissertation (manufactured by Dexmat™) is stated by the manufacturer to have been produced from wet spinning, carbon nanotube (CNT) fibres can be constructed in a number of ways.

98. Coagulation spun fibres [33], and [34] are created by the injection of a CNT dispersed solution into a polymer solution. The polymer serves as a binder for fibre formation, however the presence of the polymers between CNTs reduce the mechanical, thermal and electrical properties of CNT fibres spun this way.

99. Liquid-crystalline spinning [35] uses the nature of the CNT solution to form a liquid crystal under certain conditions, which in turn leads to highly oriented fibres. However, the difficulty in creating the correct liquid crystal conditions lead to a relatively slow rate of production for these kinds of fibres. Likewise, as the fibres are simply aggregates of CNTs, they generally have poor properties in comparison with fibres created by other techniques.

100. Forest spinning [36] and [37] of CNT fibres, are created by vertically drawing and twisting “forests”, or “mats”, of CNTs initially grown on silicon wafers. Fibre properties depend on where the CNTs are positioned on the wafer, as such properties vary across samples.

101. Direct spinning [38] and [39], utilises an injection of a liquid carbon source into a high-temperature furnace. The CNT fibre exits through the bottom of the furnace, and provides a very high spinning rate of roughly 20-30 m/min. The cleanliness of the source carbon and chamber all contribute to the final properties of the fibre.

102. It is reported in [40] that dipole antennas manufactured from dry-spun CNT fibres have low radiation efficiencies (~ 26% of equivalent sized copper dipoles), and that even a CNT rope 5 times thicker than an equivalent copper wire would be at most only ~65% efficient at the 2.4 GHz frequencies. Theory however, [40] indicates that the performance of any antenna comprising CNT fibre should scale with the density and conductivity of the CNT fibre utilised. As such, [41] show that using densely packed but moderately conducting antennas comprising wet-spun CNT thread match the absolute performance of equivalently thick copper antennas at a range of frequencies.

Chapter 2: Methodology, Results & Analysis

103. Introduction

104. This chapter contains descriptions of the methodology and data analysis utilised in the project in order to determine whether the application of design improvements, and utilisation of CNT fibre, will enable any reduction in the efficiency of individual SRR antennas. Where possible, a brief description of the various methods is given before any results are analysed, however as certain methods require a more detailed explanation, those particular methods are contained within their own appendices.

105. The first section in this chapter shows the return and transmission loss results obtained from computational modelling of a standard configuration copper SRR via HFSS (High Frequency Structure Simulation). The purpose of this initial section is to replicate the simulated and experimental results seen in the papers reviewed in the previous chapter. The results presented, while not able to recreate either with complete accuracy, give us some confidence that the software, and the simulation setup itself, is somewhat capable of accurately replicating previous results. In subsequent sections, these initial simulations are built on via the application of measured real-world electrical conductivities.

106. The implementation of the design improvements to the computational modelling is seen to give results contrary to what the literature reports and, as such, the lack of confidence in these results means they are not used to influence prototype production. Further modelling however is then conducted alongside the creation of a series of prototypes. One of these prototypes are compared against the results of the modelling and the modelling is shown to require substantial refinement.

107. Finally, of the prototypes constructed, two (one copper, and one CNT fibre), are taken into an RF anechoic chamber where transmission losses are analysed, and gain measurements are calculated, enabling a determination as to whether the substrate modifications, and CNT fibre SRRs show any improvement over equivalent sized copper SRRs.

108. The replication of previously reported simulated and experimental results.

109. The replication of previously reported results was conducted using ANSYS HFSS (2019, R1). The ANSYS HFSS program uses a time domain finite element analysis to provide solutions to Maxwell's equations.

110. The initial model setup involved the replication of the standard SRR configuration, shown below. The rings are comprise copper, and the substrate is made from FR4_epoxy (a type of glass). For brevity, the simulation setup is described in detail within appendix 2.

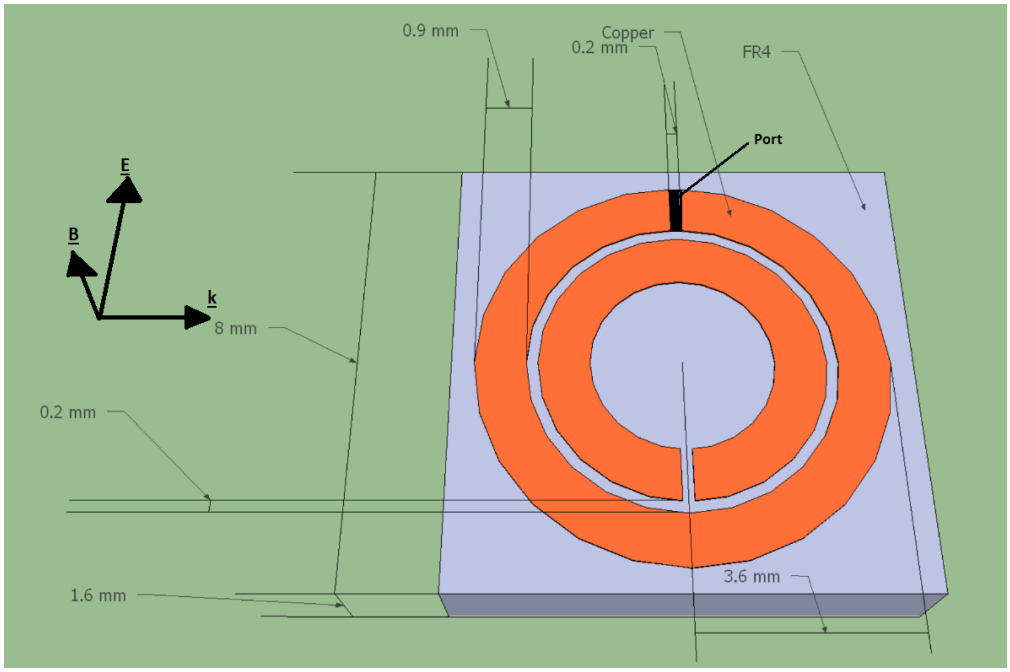

111. *Figure (7): SRR on substrate*

112. Both materials are taken from the internal HFSS materials library. Properties below;

Material	Relative permittivity	Relative Permeability	Bulk Conductivity
Copper	1	0.999991	58,000,000 Siemens/meter
FR4_epoxy	4.4	1	0 Siemens/meter

113. *Table (1): material properties taken from the internal HFSS materials library.*

115. *Note: HFSS utilises a range of material properties including the material thermal conductivity, and thermal expansion co-efficient. However the most important properties for the capacitance and inductance in any dielectric are the inherent relative permittivity and permeability.*

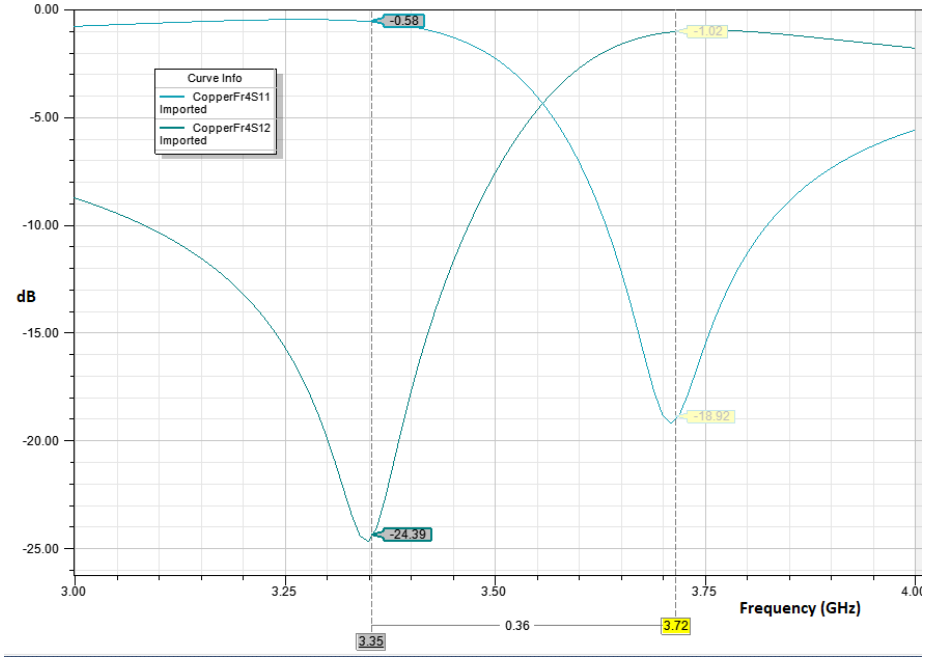

116. *Figure (8): The reflection losses ($S_{1,1}$)) right, and transmission losses ($S_{1,2}$)) left, of the standard SRR configuration*

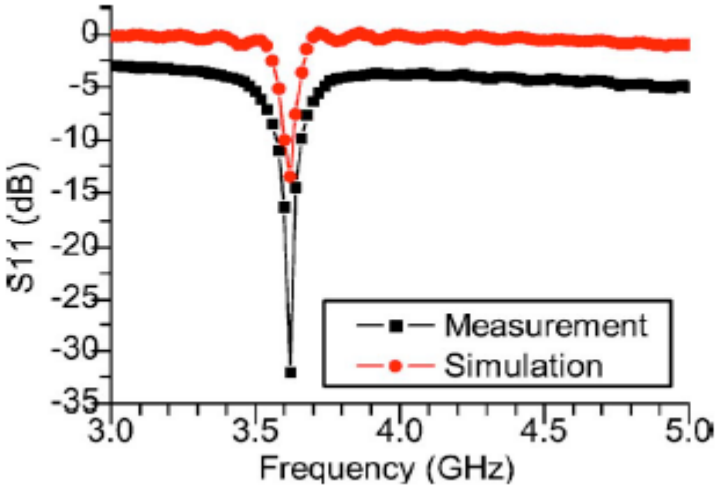

117. *Figure (9). ($S_{1,1}$)) of the SRR antenna, measurement, and simulation* [42]

118. *Note: $S_{1,1}$),and $S_{1,2}$) refer to plots of reflection losses and transmission losses respectively.*

119. ## Simulation results analysis

120. The results shown in the figures above are roughly similar to the real wold and simulation results seen in the published literature. The primary difference between the simulations conducted for this dissertation and the results presented in published literature are the differences in resonant frequencies. The results above show a ≈100 MHz difference from the experimental and published results. While the author is unable to explain the difference in frequencies (as the simulation setup should be identical), the differences in return loss frequencies between results would appear to be notable but within an acceptable margin.

121. ## Materials analysis

122. While the purpose of this project is to determine whether COTS CNT fibre can be utilised in individual SRR antennas, it is expected that the electrical resistivity/conductivity will have a large influence on the antenna operation, as such, the primary materials analysis performed for this project involved the measurement of electrical resistivity of both copper wire and CNT fibre.

123. The resistivity and conductivity of copper is well known and well reported [43], however, the quality of any copper sample has the potential to increase or decrease this property. Similarly, while the manufacturer of the CNT fibre (Dexmat™), provided a value of line resistivity for the samples purchased, as accurate information as possible for all samples was required to input into the computational simulations, in order to influence prototype production.

124. Following these results, Raman spectroscopy was then performed on a number of CNT samples and the CNT fibre in order to help explain the measured resistivities/conductivities. While, as will be seen later, the low conductivity of the CNT fibre (relative to copper), doesn't necessarily impede the usage of CNT fibre as antenna elements in individual SRR antennas, the results indicate areas of improvement in the CNT fibre manufacturing process

which, if acted upon, should provide improved material properties for utilisation in the RF domain.

125. The four-point method for electrical resistivities/conductivities

126. The four-point probe method was applied to the three CNT fibres and copper wire to determine electrical resistivities and conductivities. Measurements were conducted using a Keithley 2700 multimeter. This method provides an advantage over the standard two-point (2 probe) method for determining electrical resistance via the separation of current and voltage electrodes. This separation eliminates the lead and contact resistance from the measurement and allows precise measurement of very low electrical resistances.

127. In this measurement method, current is supplied by a pair of current leads (indicated by number 1 and 4 in the figure 10). A pair of voltage leads (2 and 3 on the figure) are connected at a smaller separation distance than the current leads. These voltage leads do not include the voltage drop incurred by the current leads and any voltage drop between the voltage leads and sample should be negligible.

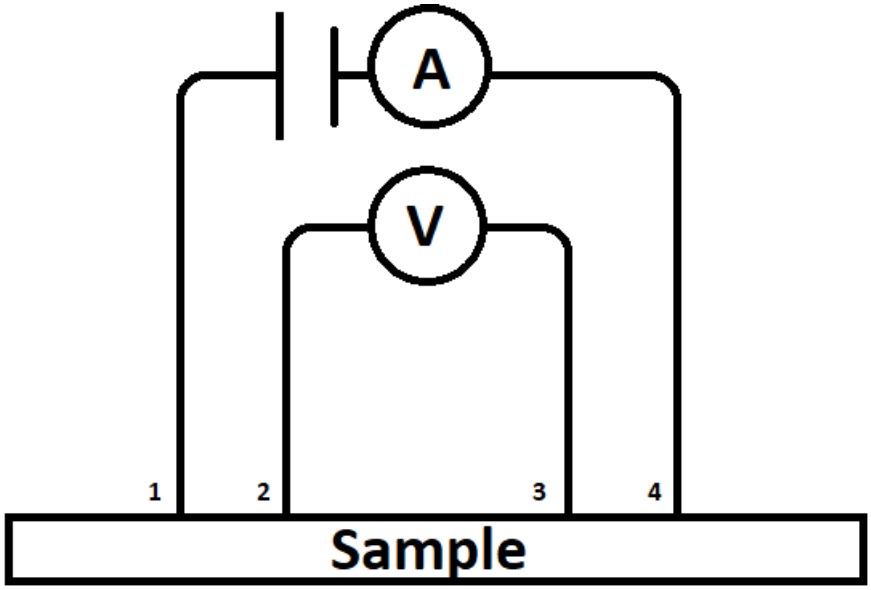

128. *Figure (10): The four point method example setup. Current leads are indicated by numbers 1 and 4, and voltage leads are indicated by numbers 2 and 3 on the figure.*

129. *Electrical Conductivity/resistivity measurements*

130. Resistance measurements were taken via the multimeter at five different separation distances per sample. The table below shows the averaged resistance, resistivity, and line resistance measurements. Both the current and voltage leads were connected to each sample via crocodile clips. Each reading was taken after 30 seconds as the initial resistance measurements tended to fluctuate after initial contact with the voltage leads, possibly due to the mechanical movement of the samples, or potentially via self-inductance of each sample as the voltage leads are moved through the electric field surrounding the sample.

Sample	Diameter, (μm)	Average measured resistance (Ω)	Resistivity (Ω.m) average	Line resistance (Ω/meter) average	Manufacturer stated (*) line resistance (Ω/meter)	Conductivity (σ/m) average
CNT Fibre	125	5.317±0.168	$2.092 \times 10^{-7} \pm 0.11$	17.05 ±0.538	17*	4.778×10^{6}
	250	0.969±0.010	$2.147 \times 10^{-7} \pm 0.02$	4.373 ±0.032	4*	4.658×10^{6}
	500	0.411±0.012	$2.116 \times 10^{-7} \pm 1.24$	1.078 ±0.537	1.3*	4.725×10^{6}
Copper wire	125	0.477±0.014	$1.907 \times 10^{-8} \pm 0.007$	1.554 ±0.0475	1.36[63]	5.244×10^{7}
	250	0.116±0.071	$1.811 \times 10^{-8} \pm 0.008$	0.369 ±0.0138	0.34[63]	5.520×10^{7}
	500	0.028±0.007	$2.550 \times 10^{-8} \pm 1.97$	0.130 ±0.0733	0.08[63]	3.922×10^{7}

131. *Table (2): Electrical resistivity measurements of the CNT fibre and copper wire at equal (average) radii.*

132. As can be seen, the measured electrical conductivity of the fibre is ≈ 10 times less than the measured conductivity of the equal (average) diameter copper wire.

133. ## Raman Spectroscopy to determine CNT, and CNT fibre nanotube diameter, and (n,m) assignment

134. Two nanotube samples manufactured by HiPCO™, and Carbolex™, alongside the CNT fibre manufactured by Dexmat™ with 250 μm (average diameter), were tested under all three laser wavelengths. These individual samples of CNTs were tested alongside the Dexmat™ CNT fibre as extensive testing has been performed and reported against each of these samples [25], thus allowing comparison of the test results and data analysis techniques with previous results.

135. The Dexmat™ CNT fibre was purchased in 3 average diameters (125 μm, 250 μm, and 500 μm. As there was no indication the different fibres were produced using different methods, (indeed all 3 fibre diameters appear to have been woven from thinner fibres), the Raman spectroscopy was performed on the 250 μm average diameter fibre only. The data taken from all samples is analysed via curve fitting, using the Magicplot student edition program. The curve fitting applied to the RBM measurements allow us to determine the peak Raman shift positions of any individual carbon nanotubes in the samples.

136. The peak positions are used to determine the range of tube diameters (d_t) in a sample. In turn, using $\mathbf{C}h = n\mathbf{a}_1 + m\mathbf{a}_2$ (equation 5) (where $\mathbf{C}h = \pi d_t$), all possible (n,m) assignments are determined alongside their relationship with d_t. This is then referenced against the information from [44]. This referencing indicates the energy levels associated with each (n,m) assignment, and referencing against a Kataura plot [30] is then used to determine the (n,m) assignment per nanotube diameter. The (n,m) assignment allows us to determine whether each individual nanotube is metallic or semi-conducting . Table 3 (below), shows the laser wavelength, wavelength photon energy of each sample, alongside the tube diameters, chirality and metallic or semi-conducting properties of all samples tested.

Sample Type (CNT or Fibre)	Wavelength (nm)	Wavelength photon energy (eV)	Diameter (nm)	Chirality (n,m)	Metallic or semiconducting
Carbolex	785	1.579	1.67±0.01	19,2	s
Carbolex		1.579	1.51±0.02	12,7	s
Carbolex		1.579	0.81±0.005	9,1	m
Carbolex	633	1.958	1.53±0.01	16,4	s
Carbolex		1.958	1.35±0.02	10,7	s
Carbolex	488	2.54	1.56±0.003	17,3	m
Carbolex		2.54	1.38±0.01	13,5	s
Hipco	785	1.579	0.92±0.02	10,2	s
Hipco		1.579	1.05±0.02	13,0	m
Hipco		1.579	1.09±0.01	13, 0	m
Hipco		1.579	1.21±0.03	11,4	s
Hipco		1.579	0.94±0.02	10,2	s
Hipco	633	1.958	0.95±0.01	12,6	m
Hipco		1.958	0.86±0.01	12,6	m
Hipco		1.958	0.82±0.01	10,0	m
Hipco		1.958	1.13±0.03	14,1	s
Hipco		1.958	1.28±0.01	15,1	s
Hipco	488	2.54	1.09±0.01	13,1	s
Hipco		2.54	0.96±0.04	9,3	s
Hipco		2.54	1.01±0.01	9,9	m
Hipco		2.54	1.13±0.06	9,9	m
Hipco		2.54	1.23±0.03	12,4	s
Fibre	785	1.579	0.91±0.01	10,0	m
Fibre		1.579	1.53±0.01	19,1	s
Fibre		1.579	2.02±0.02	18,9	m
Fibre		1.579	1.04±0.02	7,7	s
Fibre	633	1.958	1.63±0.01	21,0	m
Fibre		1.958	1.11±0.01	14,2	s
Fibre	488	2.54	1.88±0.01	18,6	m
Fibre		2.54	1.6±0.01	12,9	m
Fibre		2.54	2.42±0.01	21,10	s
Fibre		2.54	1.38±0.01	13,5	s
Fibre		2.54	1.11±0.03	8,6	m

137. *Table (3): CNT diameters, determined via the Raman spectroscopy method.*

138. From the Raman results of the CNT fibre in table 3, we can see that there are a variety of chiralitys indicating a mix of both metallic and semi-conducting nanotubes per sample tested. As mentioned in the literature review any boundary interface change, (such as the boundary between any type of CNT), will disrupt the propagation of any electrons through a material. This will therefore reduce the drift velocity below ballistic speeds, and reduce the conductivity. Similarly, while the results presented do not indicate the lengths of the

individual CNT's comprising the fibre, we can assume from the mixture of tubes that there will probably be a void between each tube, which any electrons in motion will have to tunnel across.

139. The void, or average tube spacing in a fibre sample, reported in [45] is given as 3.39 nm. These voids, alongside any defects in the CNT lattices, will tend to reduce the electrical conductivity of any CNT fibre sample, and should go towards explaining the low conductivity measured.

140. Application of measured electrical conductivities to the standard SRR design, modelling and simulation of passive CNT Fibre SRRs

141. The results of the electrical conductivity measurements from the previous section are applied to the original SRR design to determine any change in resonance frequencies.

142. Further to this, models are created and simulated in HFSS.

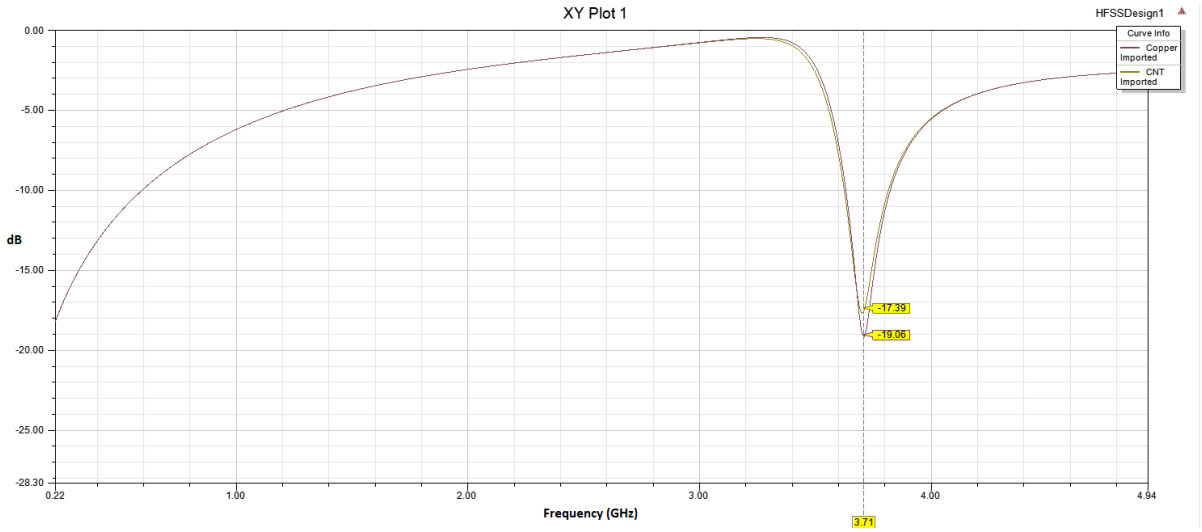

143. *Figure (11): A return loss plot of the standard SRR comprising copper and CNT fibre.*

144. While difficult to see from Figure 11, the simulations indicate a lower return loss from the CNT fibre when the measured electrical conductivity is applied. The CNT fibre shows a return loss of -17.39 dB, while the copper SRR model shows a return loss of -19.06 dB. No significant increase in bandwidth is seen (bandwidth measured at – 10 dB). It must be noted that accurate simulations in HFSS rely on more than the electrical conductivity of the materials. The mass density, relative permeability, and permittivity are properties which will significantly alter the results from inputted models. While the mass density is stated by the manufacturer (1300 kg/m^3), the other two properties are unknown. As the modelling of CNT SRRs without these materials properties is likely to give false results, the modelling from this point forwards shall focus on copper SRRs only, as the material properties in the material library is likely to be somewhat accurate.

145. The modelling and simulation of design improvements.

146. The design improvements, mentioned in chapter 2 (paragraphs 24 - 48) are applied here to the HFSS simulations.
In this sub-section, improvements are applied to the standard SRR configuration where the conducting elements are made of copper, and the return loss ($S_{(1,1)}$), and transmission loss

($S_{1,2}$)) results are recorded and compared against the modelling from the previous sub-section.

147. With reference to the HFSS materials library, ferrite was chosen as the substrate for both the simulations and the subsequent prototype build. The material properties of ferrite given by the HFSS materials library include a relative permeability, μ_r = 1000, and a relative permittivity, ε_r = 12. Other materials considered include, iron (μ_r = 4000, and ε_r = 1), sea water (μ_r = 0.9991, and ε_r = 12), and while these materials are likely to have a lower electrical conductivity than copper, they may have a higher electrical conductivity than the CNT fibre . As ferrite is solid, easy obtainable, cheap, and safe to handle and has a relatively high value of μ_r, and ε_r it was chosen as an ideal material for the substrate.

148. The first set of simulation results show the original substrate, consisting of FR4-epoxy replaced with a ferrite substrate of the same dimensions.

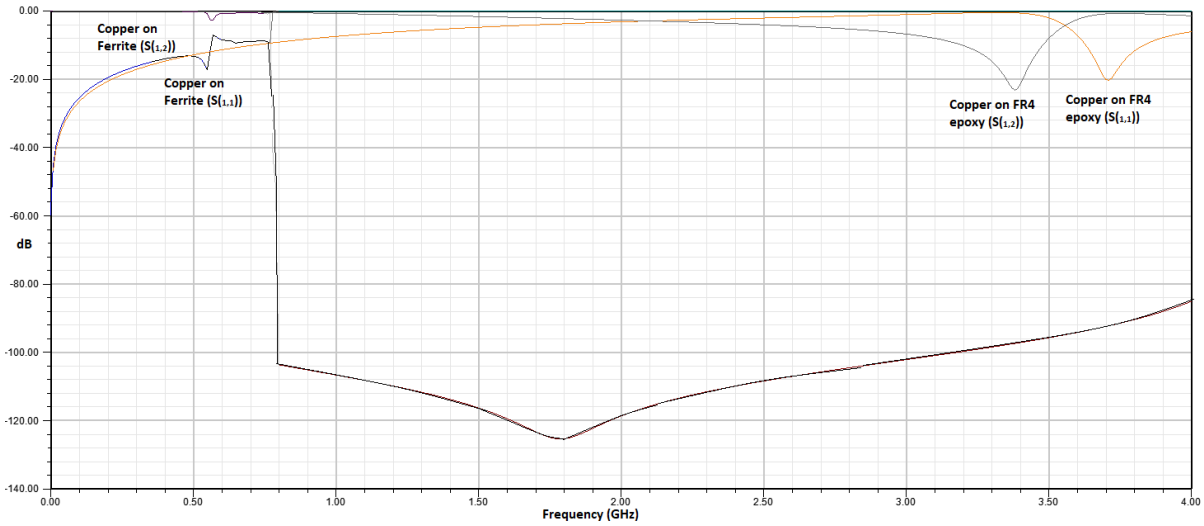

149. *Figure (12): The return loss ($S_{1,1}$)) and transmission loss ($S_{1,2}$)) results of the original SRR design with an FR4-epoxy substrate, alongside the replacement ferrite substrate results. Note: The copper on FR4-epoxy results as seen in figure 11 are shown far right.*

150. Significant transmission losses are indicated when the FR4-epoxy substrate is replaced with ferrite at frequencies above 770 MHz. While this may indicate a large bandwidth above this frequency, the lack of any significant return loss somewhere within this bandwidth may be due to a significant amount of energy being absorbed into the substrate on the path from port 1 to port 2. Likewise, the geometry of the simulation setup itself may present a problem. As the SRR element is situated in a very narrow waveguide (as per the method indicated in appendix 2), the volume taken up by the substrate, in addition to the apparent large loss tangent of the substrate at these frequencies, alongside the boundary conditions applied, may all combine to prevent significant amounts of energy from passing through the substrate, thereby artificially increasing the transmission losses. The huge transmission losses may also indicate a problem related to the wide range of frequencies across the simulation spans. A simulation across this range of frequencies requires both a large boundary external to the antenna element equal to ¼ λ, where the boundary = 7.5 m at the lowest frequency of 10 MHz, and also requires a very fine tetrahedral mesh inside both the ferrite and copper at higher frequencies. HFSS may have had trouble refining the overall mesh of both at the 700 MHz – 800 MHz boundary and, similarly, material properties inherent to ferrite in the HFSS materials library may require a far denser mesh than would be expected for other materials.

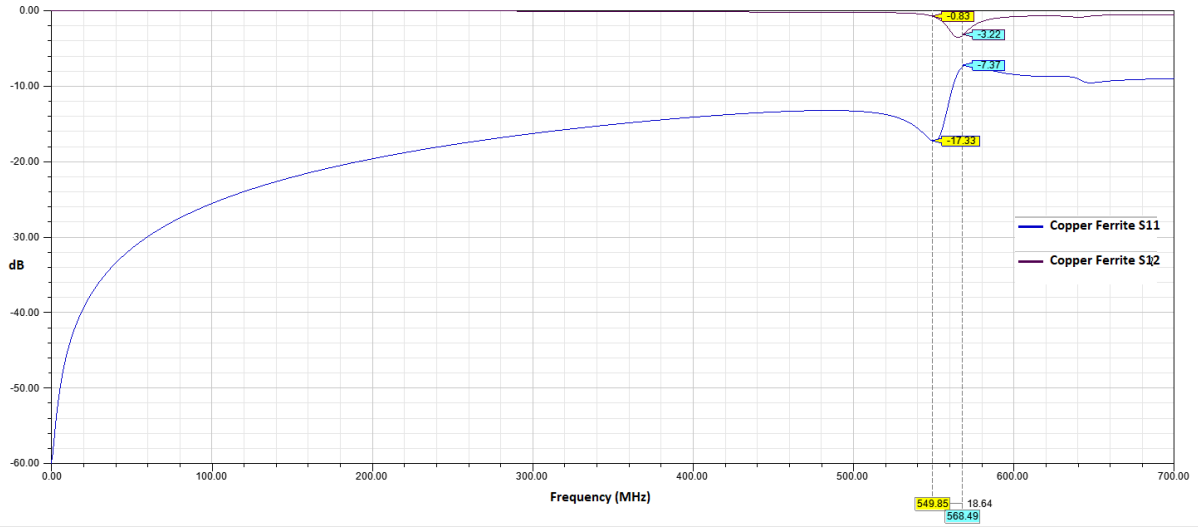

151. *Figure (13): Detail view of the return loss and transmission loss results of the original SRR design with a ferrite substrate.*

152. While difficult to see due to the magnitude of the transmission loss in the previous figure, a low return loss frequency at ≈ 550 MHz is seen in a detailed view of the lower frequencies, indicating the addition of a ferrite substrate to the standard SRR configuration has a significant impact on the return loss frequencies of an individual SRR.

153. One conclusion which may be drawn from this set of simulation results are the potential pitfalls of simulating an individual SRR element in a waveguide. While a waveguide is somewhat useful for determining the resonant frequencies of an antenna element (as shown by the agreement in frequency if not return loss readings in simulated and experimental results previously published). In particular, the behaviour of an element in a waveguide may be considered to be the behaviour of one element in an infinite array. This particular setup then, may not be useful for accurately simulating individual antennas.

154. In order to attempt to gather more accurate simulations of any prototypes to be constructed, the excitation port is therefore moved onto the outer ring of the SRR, as the prototype antennas will be excited from a coaxial cable connected directly to the outer ring of an SRR rather than be excited and driven from an external EM source as simulated so far.

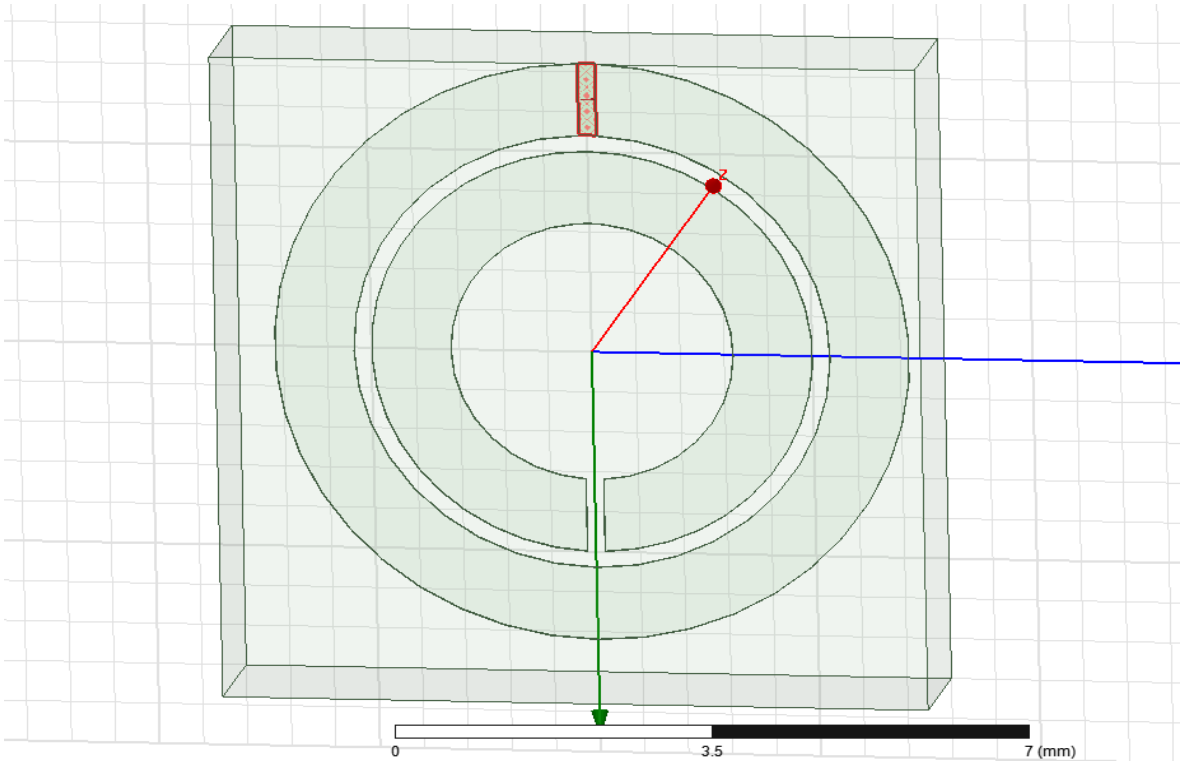

155. *Figure (14): The standard SRR configuration with feed point placed in the split in the outer ring, and ferrite substrate. The feed point is highlighted in red. The integration line (line of current) heads across the feed (right to left in this orientation).*

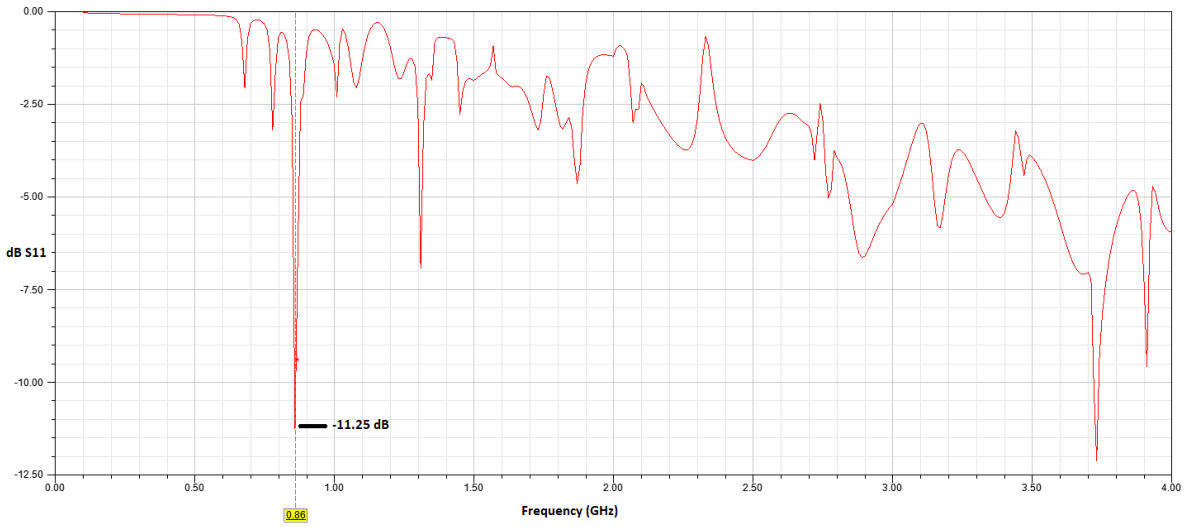

156. *Figure (15): The return loss results ($S_{1,1}$)) for a standard configuration SRR with feed point moved to the external ring, and a 1.6 mm ferrite substrate.*

157. As the simulation now consists of one port (the feed point), the simulations consist solely of return loss ($S_{1,1}$) plots. In addition, the models were modified with a higher resolution mesh and a reduced radiation boundary size (equal to ¼ λ at 400 MHz). We can see from the figure above that the lowest return has shifted from ≈0.55 GHz to 0.86 GHz, and the return loss magnitude is equal to –11.25 dB in comparison with – 17.33 dB from an external EM source (Figure 13).

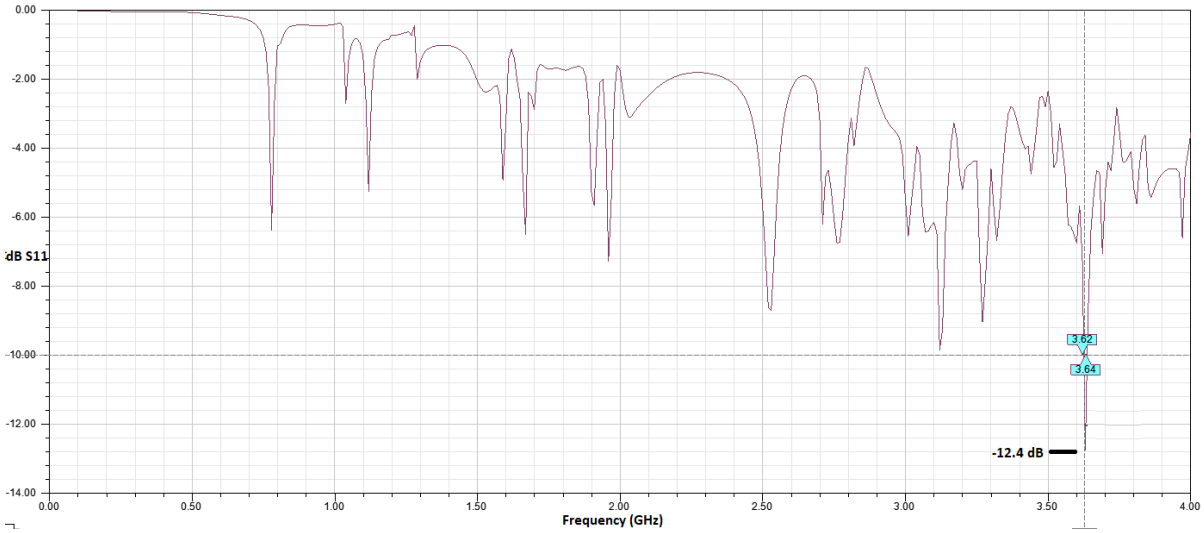

158. *Figure (16): The return loss ($S_{1,1}$)) of the standard SRR configuration with the feed point in the external split, and a ferrite substrate with the substrate thickness increased to 2 mm.*

159. The modelling results indicate that an increase of ferrite substrate thickness from 1.6 mm to 2 mm leads to an increase in return loss frequencies from 0.86 GHz (at 1.6 mm substrate thickness) to 3.64 GHz (at 2 mm substrate thickness).

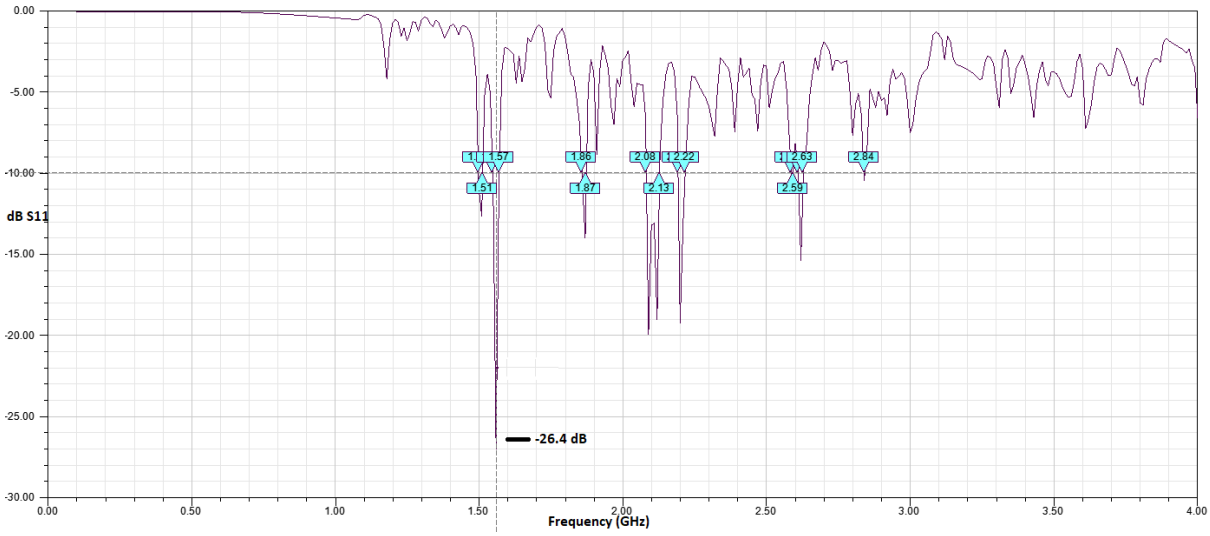

160. *Figure (17): The return loss ($S_{1,1}$)) of the standard SRR configuration with feed point in the external split, a 1.6 mm thick ferrite substrate and 0.2 mm ring widths.*

161. The results from the figure above indicate a reduction in the thickness of each ring (from 0.9 mm to 0.2 mm), where the ring height from the ferrite substrate is kept at 30 µm, will provide the lowest significant return loss (at losses < 10 dB) at 1.51 GHz. This is a significant frequency reduction in comparison with the standard SRR configuration return loss (< 10 dB) of 3.6 GHz.

162. Various conclusions can be drawn from the results presented above. The simulation of an individual SRR is best simulated with a feed point attached to the antenna itself, rather than being simulated by an infinite array approach. Increasing the thickness of a substrate attached to an SRR will not necessarily decrease the return loss frequencies and, similarly, reducing the thickness of the rings in an SRR, will likewise, not decrease the return loss frequencies.

163. If these simulations are taken at face value, they would seem to contradict the design decisions indicated in the published literature, as we would expect a subsequent decrease in associated return loss frequencies by the increase in substrate thickness.

164. As a result of the conclusions drawn from the modelling to this point, and the lack of any physical test results to determine the accuracy of the simulations, it was decided to continue using the modelling software by modelling the prototypes for the physical testing and simultaneously creating and testing prototypes. The results of both are compared, and should allow a determination as to whether the modelling set up "as is" is capable of accurately predicting the future behaviour of any modified split ring designs.

165. Prototype production

166. The physical dimensions of the prototypes modelled in HFSS were based upon the materials procured for use in the construction of real-world prototypes.

167. Materials used for modelling and construction include;

- 10 mm diameter x 5 mm thickness ferrite disc
- 250 µm thickness copper wire (of various lengths)
- 250 µm (average diameter/thickness) Dexmat^{tm} CNT fibre (of various lengths)

168. Figure 18 (below), shows a model of the setup with material dimensions (created in Sketchup for illustration), and Figure 19 shows the return loss created by HFSS of the SRR in Figure 18.

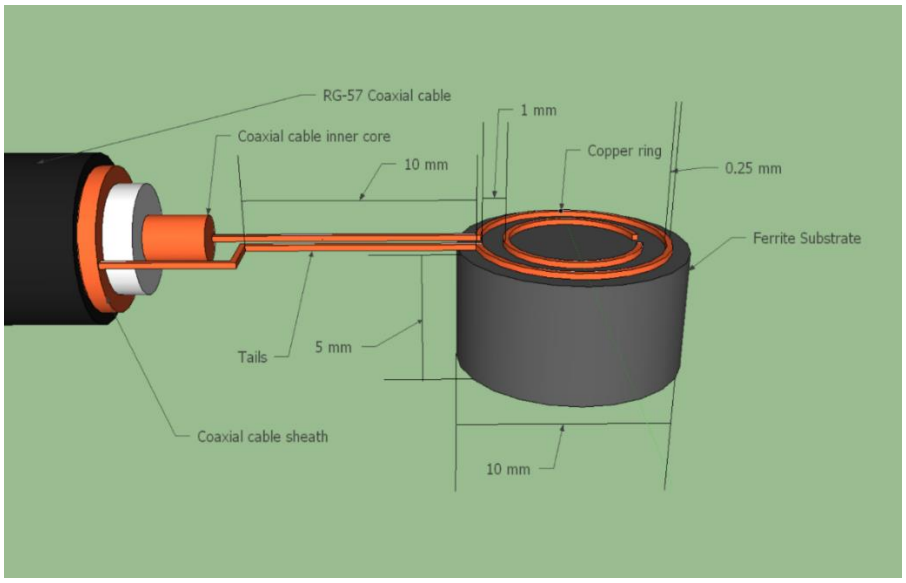

169. *Figure (18): A copper SRR prototype setup on a ferrite substrate.*

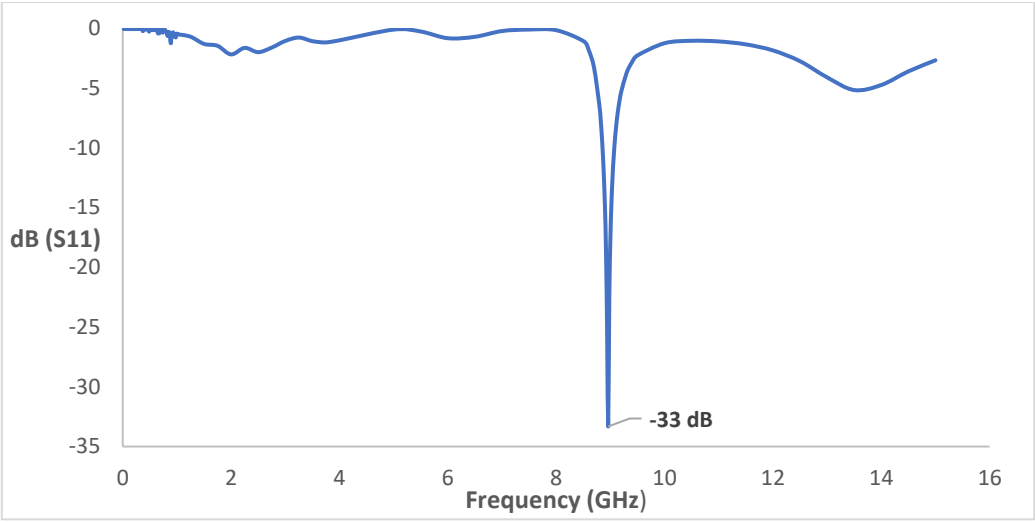

170. *Figure (19): The Return loss ($S_{1,1}$)) plot for a 7 mm OD copper SRR, as seen in figure 18;*

171. In contrast with the large number of return loss frequencies from the previous modelling, the only significant return losses seen in the figure above are at 8.9 GHz. As no return loss was seen from this modelling in the 400 MHz to 4 GHz frequency range, the range was extended to 16 GHz. Likewise, the modelling setup broken down into 4 sections of a 4 GHz frequency range each (400 MHz to 4 GHz, 4 GHz to 8GHz, etc.).

172. Six prototype SRR antennas were constructed. Five of the conducting elements were constructed from copper, and one from the CNT fibre. All conducting elements (copper and nanotube fibre) were laid upon a disc of ferrite unless otherwise stated. The ferrite discs have dimensions 10 mm outer diameter (OD) x 5 mm thickness.

173. The initial copper prototype comprised 0.25 mm thick copper wire on a ferrite substrate, with an OD of 10 mm. The gap between the outer ring and inner ring was approximately 1 mm (+/-) 0.2 mm, with an inner ring split width of 1mm (+/- 0.2 mm) and feed point split width (at minimum/on the substrate) of 1.2 mm (+/- 0.2 mm). The ferrite substrate comprised a 10 mm OD by 5mm thick disc. The copper was adhered to the substrate using COTS (Commercial off the Shelf) adhesive (Gorilla glue). The feed point tails are approximately 10 mm long, and the feed point is soldered to an RG-57 coaxial cable, as per figure 19.

174. Equal sized copper split rings were placed on a paper substrate to gain any experimental evidence of the effect of the substrate on the resonance frequency.

175. Similarly, a 7 mm OD SRR on another 10mm diameter/5mm thick ferrite disc with equal split distances and gap widths as the 10 mm outer dimeter prototype was constructed and tested to experimentally determine any changes in resonant frequency by changes in the geometric properties of the SRRs. Further in order to test whether a larger amount of the substrate encasing a prototype would be able to store a larger amount of energy in the magnetic field created by the prototype, and therefore decrease the resonance frequency, a modification to the 7 mm OD prototype involved the placement of a secondary 10 mm OD x 5 mm thickness ferrite disc on top of the prototype.

176. Two final prototypes were constructed for transmission loss testing, one from copper and one from carbon nanotube fibre. The copper and CNT NF outer ring diameters are 8.5 mm with a 0.25 mm wire/fibre (average) diameter, with equal split, gap and feed point dimensions to the other prototypes. This outer ring diameter was dictated by the dimensions of the equipment to hand during the NF manufacturing process.

Prototype Conduction Material	Ring Thickness (mm)	Outer Ring Diameter (mm)	Substrate	Split/Gap width (mm)
Copper	0.25	10	Ferrite	1 (+/-) 0.2
Copper	0.25	10	Paper	1 (+/-) 0.2
Copper	0.25	7	Ferrite	1 (+/-) 0.2
Copper	0.25	7	Ferrite *2	1 (+/-) 0.2
Copper	0.25	8.5	Ferrite	1 (+/-) 0.2
CNT Fibre	0.25	8.5	Ferrite	1 (+/-) 0.2

177. *Table (4): Prototype properties table*

178. Fibre, by its very nature, is not particularly rigid, and will not hold the shape of a ring. The inner ring was therefore adhered to the outside of a solid plastic (PVC) cylinder of dimensions 7 mm OD x 1 mm height (see figure 20, below). The outer fibre ring was then adhered to the outside of a hollow plastic cylinder, of 1 mm thickness and approximate dimensions 8.25 mm OD, 7.25 mm inner diameter (ID), with 2 mm height. During manufacture of this prototype (in a fume cupboard using appropriate personal protective equipment), both the external and internal fibre rings were held under slight mechanical tension around the outside of their respective cylinders until the adhesive set and they were affixed securely to the plastic ring. Adhesive was applied to the bottom of each plastic cylinder and they were then stuck to the top of the ferrite disc. To fix the entire antenna in place, the bottom of the ferrite substrate was adhered to the floor of the enclosure.

179. One primary difference between the single CNT prototype and the copper prototypes is the containment of the CNT prototype inside a sealed plastic enclosure (Figure 21, next page). This is to contain any potential release of nanotubes into the atmosphere from any accidental mechanical exfoliation of the fibre during testing, as carbon nanotubes have the potential to be carcinogenic when inhaled [58]. There is no indication that the plastic utilised as the spacers for the CNT fibre, or the plastic containment box, will be anything other than transparent to RF/microwave radiation, as such they should have no effect on any test results.

180. Tails from the external fibre ring of approximately 50 mm length (per tail) were coiled around and adhered (using gorilla glue) to a 0.25 mm OD x 30 mm length copper wire, which is fed through small holes in the casing of the plastic enclosure. An RG-59 coaxial cable was then soldered to the copper wire to provide a feed point, (similar to the connection shown in Figure 26).

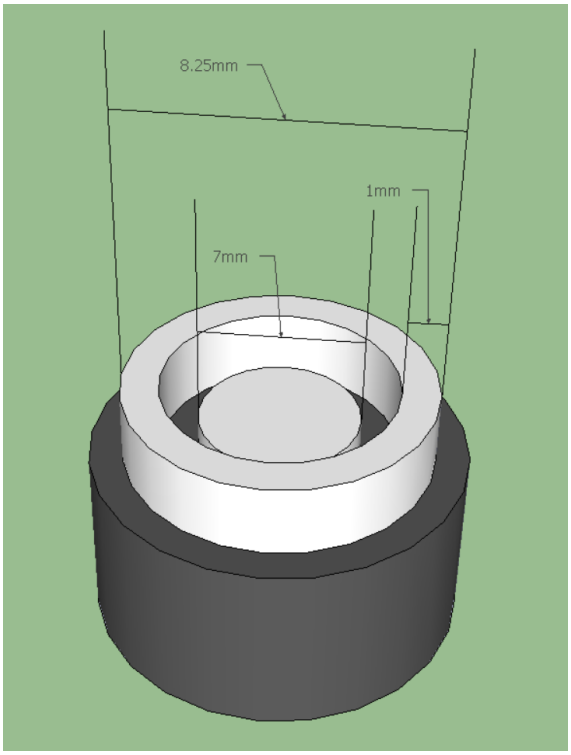

181. *Figure (20): CNT NF prototype spacers including dimensions*

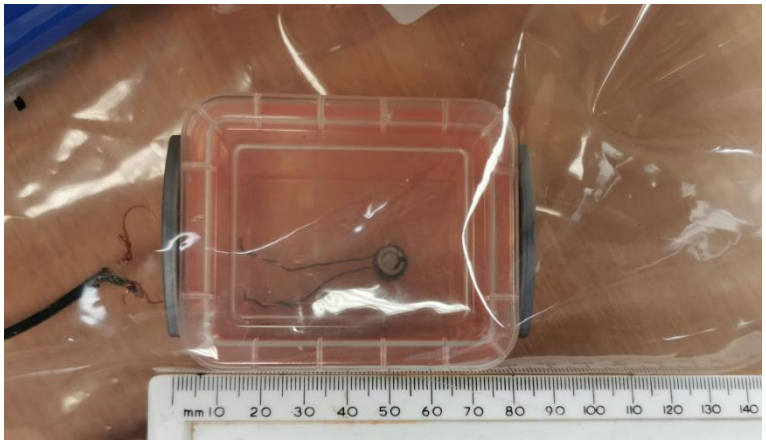

182. *Figure (21): The 8.5 mm OD CNT NF SRR prototype on ferrite substrate (In protective equipment).*

183. Return loss Results

184. Initial return losses were measured on an Anritsu 37369C vector network analyser. The return losses presented here indicate the amount of power reflected back to the network analyser from the antenna, and therefore the frequencies at which most power is absorbed into an antenna. The network analyser was set to transmit power into the prototype antennas at -30 dBm). While these plots are useful to determine at which frequencies an antenna absorbs most power, care must be taken not to assume that the antennas will inherently transmit all the power they absorb at these frequencies. Some power absorbed will inherently be lost by ohmic losses in the antenna, impedance mismatch, and even attenuated by the effect of the substrate on the conducting elements of the radiated antenna. For the purposes of this dissertation the power absorbed into an antenna but not necessarily broadcast, will be defined as the maximum antenna absorption efficiency.

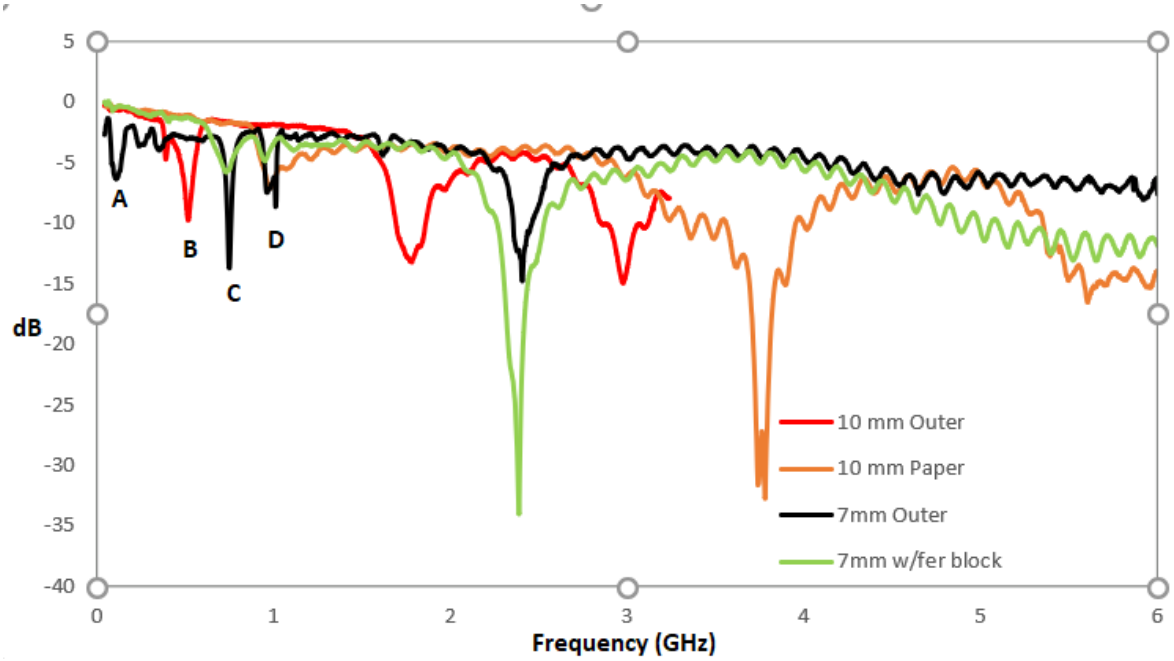

185. *Figure (22): Return loss results for a series of copper-based prototypes.*

186. The initial prototypes show a range of return losses, with the lowest absorption frequency given by the 7 mm OD on ferrite substrate, seen at 114 MHz, with a return loss of -6.5 dB (A). The next lowest absorption frequency is seen from the 10 mm OD on ferrite substrate at 512 MHz, with a return loss of -9.6 dB (B). As we would expect a smaller average ring diameter (r_0) to provide a higher return loss frequency, this is slightly unexpected. Similarly, the lowest return loss shown when a secondary ferrite block is placed atop the 7 mm OD prototype is seen at 747 MHz (C), indicating that the overall increased thickness of the substrate around a prototype will tend to increase resonant frequencies. As expected however, the lack of a substrate, as seen by the difference in the lowest return loss frequencies between the 10 mm OD on ferrite substrate, 512 MHz, (B), and the 10 mm OD on paper,952 MHz, (D), with a subsequent return loss frequency increase of 436 MHz, indicate that the addition of a substrate to an individual SRR antenna has a significant effect on resonant frequency.

187. Further analysis on the higher frequency return losses indicates that the addition of a secondary substrate (as seen in the results from the 7mm OD prototype with ferrite block on top) will significantly increase the maximum absorption efficiency of an individual SRR antenna at the secondary return loss frequencies. As we can see from the return loss frequency given by the 10 mm OD prototype with paper substrate, an individual SRR antenna solely using wires, still indicates a fairly high absorption efficiency at relatively low frequencies in comparison with the maximum width of the antenna (≈ $1/8^{th}$ of the free space wavelength).

188. In comparison with the modelling results presented for a 7 mm OD copper SRR where the only significant return loss is seen at 8.9 GHz (as seen in Figure 19), the lowest return loss on the network analyser is seen at 114 MHz. This indicates significant problems with the modelling.

189. Figure 23 (below) shows VNA results for equal sized (8.5 mm OD) copper and CNT NF prototypes.

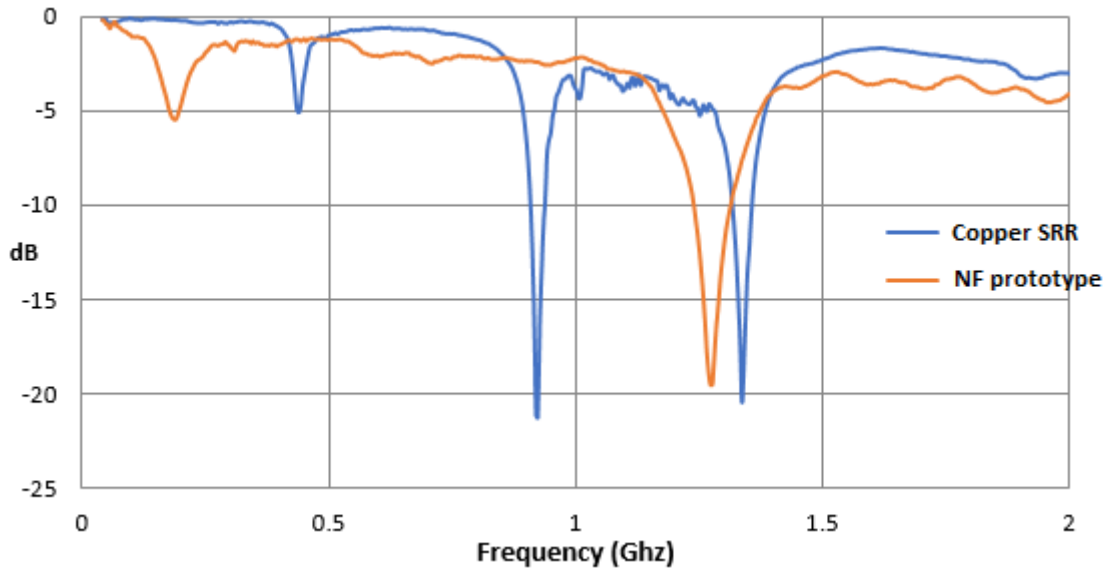

190. *Figure (23): Copper SRR, and CNT NF, 8.5 mm OD VNA (Return Loss) results.*

191. The results presented above for equal sized copper and CNT prototypes show markedly different results. The minimum return loss is seen in the NF prototype at 189 MHz, with a reading of -5.2 dB, one far larger return loss is seen at 1.27 GHz, with a reading of -19.5 dB. The lowest return loss for the copper prototype is seen at 438 MHz with a reading of -5.1 dB, while two further resonances are seen at 922 MHz and 1.3 GHz, with readings of -21.2 dB and -20.5 dB respectively. If we compare all return losses, the NF prototype consistently shows larger bandwidths at all points, and slightly deeper return losses across the frequency range.

192. We can determine the maximum absorption efficiency of each prototype. This can be determined via;

$$\eta = 1 - |\Gamma|^2$$

193. *Equation (11): The maximum antenna absorption efficiency, where Γ is the reflection coefficient* [46]

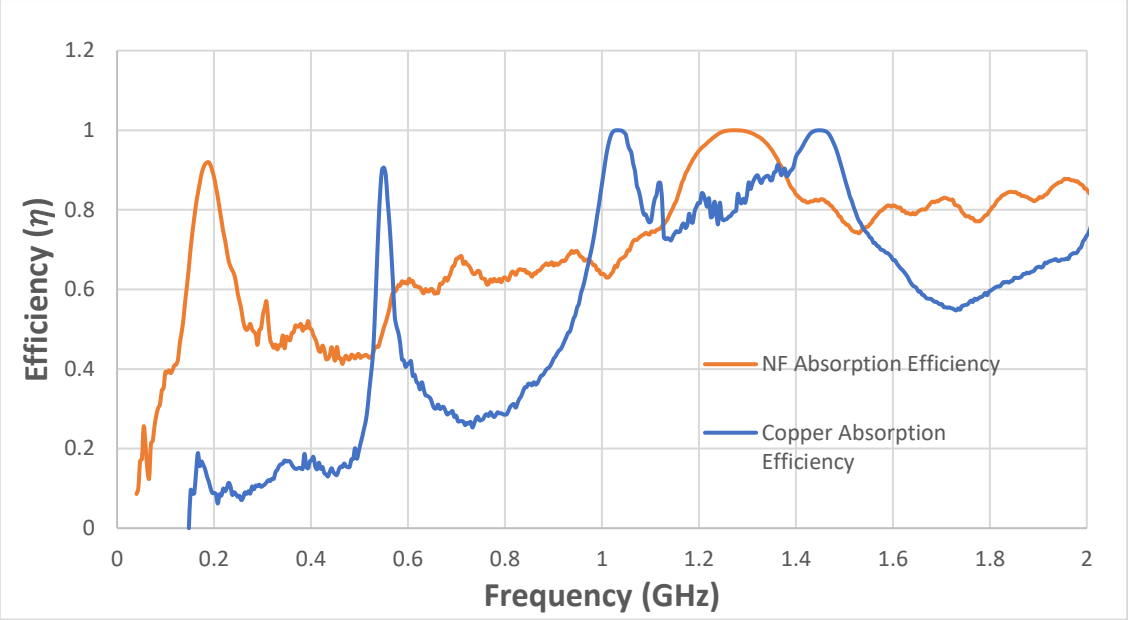

194. *Figure (24): Copper SRR, and CNT Fibre, (8.5 mm OD) maximum absorption efficiencies.*

195. From Figure 24 (above), we can see that the NF prototype has a higher absorption efficiency at all frequencies, bar the frequencies corresponding to the largest return losses as seen from the copper prototype.

196. How then can we explain the difference in absorption efficiencies between prototypes? The higher maximum absorption of the NF prototype indicates that it should be more efficient at radiating and receiving energy across a wider range of frequencies. In this case, as the measured electrical conductivity of the copper antenna is ≈ 10 times higher than the CNT fibre, we can determine that the ability of an electrically small SRR to efficiently receive and radiate is not solely dependent on the electrical conductivity of the antenna elements contained within. Clearly then, there are other differences between the fibre and wire antennas, not wholly related to electrical conductivity.

197. Some of these differences can be explained by the different internal geometry of the NF and copper prototypes. The operation of a spit ring resonator as an antenna is primarily dependent on both the inherent capacitance and inductance in the system. As the capacitance value in any capacitor is partially determined by the area of overlap between any two charged surfaces, surfaces which display larger areas of overlap will inherently display a larger capacitance.

198. It can be shown mathematically that two long parallel straight wires of a certain diameter will give larger values of capacitance than two equally long parallel plates where the plate height = wire diameter.

199. The capacitance given by a parallel plate capacitor is given by;

$$Cpp = \varepsilon_r \frac{A}{d}$$

200. *Equation (2): The capacitance between two parallel plates, where ε_r is the relative permittivity of the dielectric medium between two parallel plates, A is the area of overlap, and d is the distance between the plates*

201. While, the capacitance for a pair of parallel wires is given by;

$$Cpw = \frac{\pi \varepsilon_r l}{ln\left(\frac{d}{2a} + \sqrt{\frac{d^2}{4a^2} - 1}\right)}$$

202. *Equation (12): The capacitance between two parallel wires, where ε_r is the relative permittivity of the dielectric medium between two parallel wires, a is the radius of the wire, l is the length of the wire, and d is the distance between the wires (central point of each wire to its opposite number).* [47]

203. Thus, the capacitance between two parallel wires of the same material is then calculated to be approximately 4.2 times larger than the capacitance between two equivalent height (and material make-up) parallel plates.

204. While the surface area of a cylinder is well known, ($A = 2\pi rh + 2\pi r^2$), the surface area of a fibre is not. As the surface area of a fibre is dependent on the dimensions of the material making up the fibre, in most fibrous materials, these could be particles of various sizes and shapes, or comprise numerous strands of thinner fibre ,a generalised equation to determine surface area for a fibre is not readily available. Further complicating this in respect to the CNT fibre utilised for this dissertation is the lack of any information indicating the length or orientation of the nanotubes contained within the CNT fibre. What we can presume, however, is that the CNT fibre utilised for this dissertation will have a larger surface area than the equivalent diameter copper wire and, from the relations seen above, therefore, we can surmise that two parallel lengths of fibre will display a larger capacitance value than two equivalent diameter copper wires. Likewise, this relationship would seem to hold up for any fibrous material (related of course to some reasonable value of conductivity). In addition to this extra capacitance value between the CNT fibre rings, there will be gaps between the nanotubes comprising the fibre. In these gaps, while the area of overlap between nanotubes may be small, and the spacing distance of the same magnitude, the summation of all the individual capacitances across the entire volume of the CNT fibre may increase the overall capacitance of the system.

205. Further to this, and referring to [48] which states that the inductance component of an SRR is approximated by a single ring of radius r_0, and width c (see Appendix 1). We wouldn't therefore expect the overall inductance of a SRR as a function of the average ring radius to show much (if any) change between a CNT fibre and a copper SRR of the same outer and inner ring diameters. However, as mentioned in chapter 1, wire, (including conductive fibre we might presume), will show a certain self-inductance as a function of diameter. The CNT fibre comprises a large number of nanotubes with length (L), and diameter (d_t), with an average gap distance of 3.39 nm [49]. These nanotubes will, due to this average gap distance, comprise an effective cross-sectional area (E_a), less than the cross-sectional area of a solid wire of equal diameter. The packing density of the nanotubes in the CNT fibre is unknown, as we have no indication of the orientation or length of the tubes, however if we assume that the packing density is as dense as possible, we can approximate the minimum effective cross-sectional area of a CNT fibre.

206. If we define the radius of each "nanotube area" as being equal to half the measured average diameter of the tubes in the sample (1.51 nm), plus half the average distance between each CNT in previously measured fibres (3.39 nm [49]). The cross-sectional area of each "nanotube area" is then equal to 18.9 nm^2 (1.89×10^{-17} m^2). The percentage of this overall area

comprising the CNT is then 9.4 %. If the cross-sectional area of a 250 µm circle is then 3.93 x 10^{-10} m^2, we can then fit a minimum of ≈2.1 x 10^6 CNTs per 250 µm fibre. From this, the effective cross-sectional area of the fibre will only comprise ≈ 30.4 μm^2. This gives an effective CNT fibre diameter of 6.2 µm in comparison with a copper wire of diameter of 250 µm.

207. Utilising the equation;

$$L_{wire}(L,D) = 2L\left\{ln\left[\left(\frac{2L}{D}\right)\left(1+\sqrt{1+\left(\frac{D}{2L}\right)^2}\right)\right]-\sqrt{1+\left(\frac{D}{2L}\right)^2}+\frac{\mu_r}{4}+\left(\frac{D}{2L}\right)\right\}$$

208. *Equation (4): The inductance of a straight wire (in Henries [H]), where D is the diameter of the wire (m), L is the length of the wire (m), and μ_r is the relative permeability of the wire.* [49]

209. For equal lengths of wire/fibre at the same average thickness (250 µm, not effective thickness), the self-inductance for the CNT fibre is approximately 1.6 times higher than that of the wire. The increased self-inductance inherent to CNT fibre should therefore enable a lower resonant frequency.

210. Prototype gain testing, experimental set-up and procedure

211. Generally, the key purpose of any antenna testing is to determine the gain of the tested antenna, where the gain of an antenna is a key performance indicator which combines both the antenna directivity and the antenna electrical efficiency. The value describes how well the antenna converts electrical power into radio waves in any particular direction or vice versa. If no direction is indicated, the gain is understood to mean the peak gain, i.e. the peak value of the gain in the optimal direction. In order to measure this, transmission loss measurements were performed in an RF anechoic chamber of approximate dimensions 6 m x 4 m x 3 m (Length, Width, Height). The chamber is clad in radar absorbent material (RAM) which will severely attenuate RF/microwave signals within a certain frequency range, providing a "quiet" RF environment. The specifications of the RAM however are unknown and it is unlikely that it has much effect at low frequencies. The transmit source signal was generated by a HP 83732B signal generator, at a power level (at the signal generator) of 10 dBm (0.01 Watts). The received signal was fed from a gain calibrated helix monopole antenna to an Anritsu MS2724B spectrum analyser. Tests were performed at a series of frequencies between 10 MHz and 2 GHz.

212. The 8.5 mm OD CNT fibre (Figure 21) and 8.5 mm OD copper SRR prototypes (Figure 26) were utilised as transmit antennas, and one of two gain calibrated helix monopole antennas was utilised as receive antennas. Details on the gain calibration procedure of the helix monopole antenna, and data analysis technique are contained in Appendix 3.

213. *Figure (25): One of the helix monopoles utilised for gain measurements*

214. *Figure (26): The copper 8.5 mm OD on ferrite substrate, with plastic fixer cap*

215. Due to the range of frequencies tested in the chamber, and the potential lack of any shielding, or absorption by the chamber at the lower frequencies, there was a concern about multipath propagation. In addition, at the lower frequencies and with regards to the chamber dimensions, there was an additional concern regarding unwanted near field effects. The experimental test procedure and calculations taken in order to mitigate these effects are contained within Appendix 3.

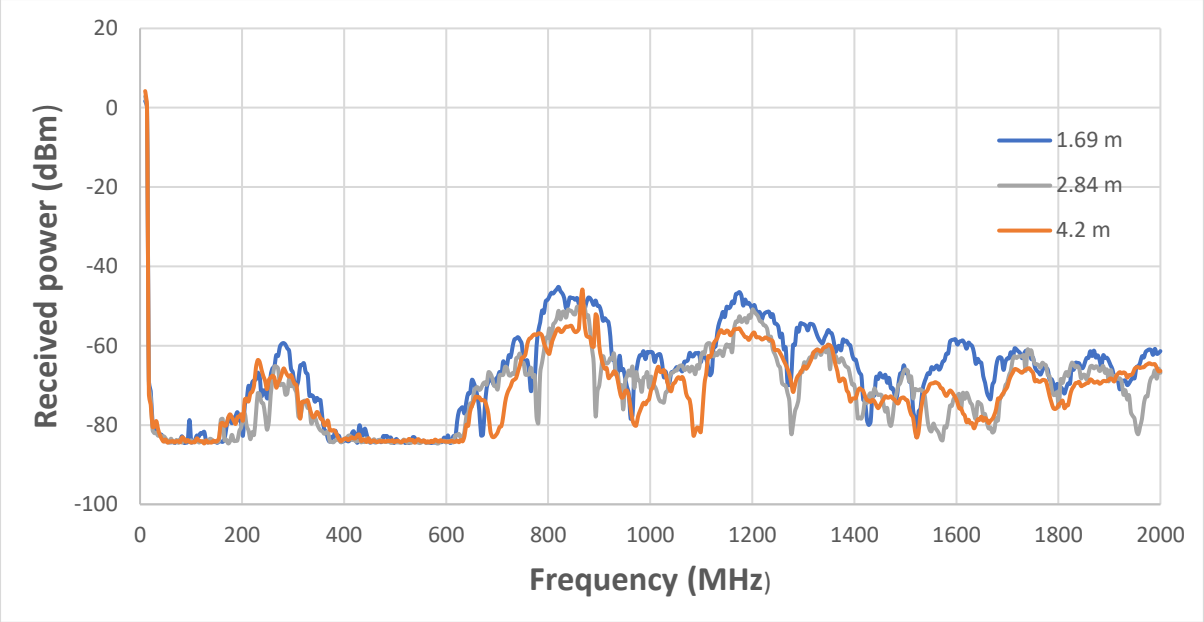

216. *Figure (27): Received powers frequency plot for the copper SRR transmitting to a helix monopole antenna.*

217. The plot above shows the powers received at a receive helix monopole antenna from the transmitting copper SRR over a range of frequencies at (a sample of) three different separation distances. At certain frequencies (237 MHz, 867 MHz, 1.945 GHz) the plot shows more power being received at the receive antenna at the furthest separation distance. This can be attributed to evidence of multipath propagation, as we would expect the receive powers to drop off as a function of increased separation distance, providing there are no secondary transmission sources close-by.

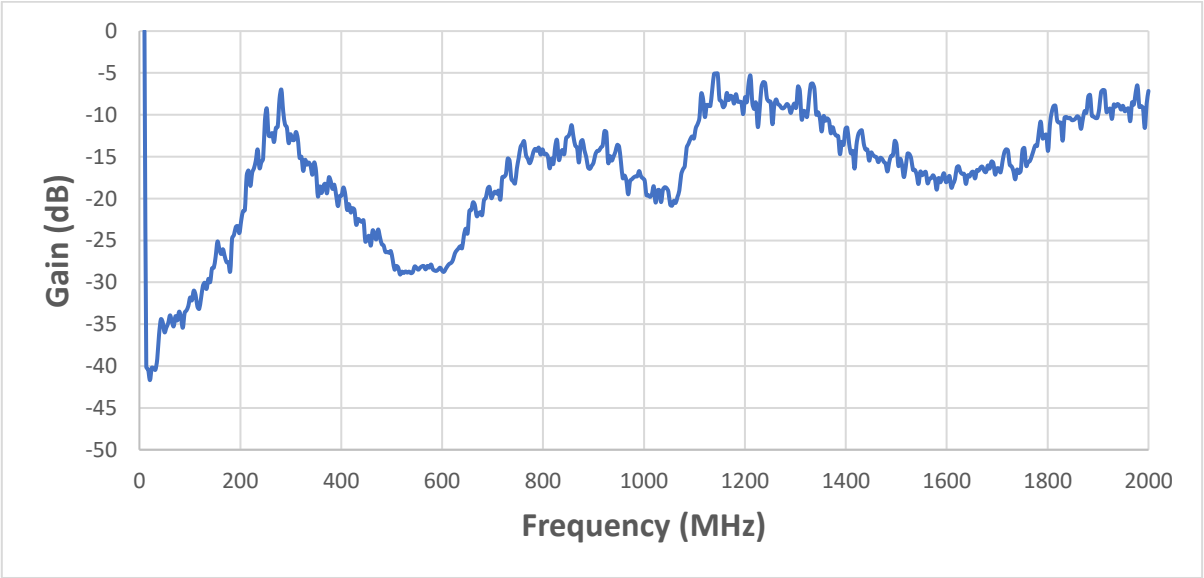

218. *Figure (28): Frequency vs Gain plot for the Helix monopole*

219. The helix monopole has an approximate length of 22.5 cm (including the extra length included in the helix). Monopole antennas are generally most resonant at frequencies equivalent to ¼ λ, as such, we would expect the highest value gain reading to be seen at around 333 MHz, with subsequent high gains to be seen at various higher integer multiples of this frequency. The highest gain at the low frequency is seen at 281 MHz, with a gain

value of -6.9 dBi, in addition to high gains seen at 856 MHz (-11 dBi), and 1.14 GHz (-5 dBi). These readings indicate that this is a ¼ λ monopole, and the extra path length accorded by the helix allows a somewhat more compact size for the structure. The gain of a ¼ λ monopole on a ground plane has been reported as 5.19 dBi [52]. The gain of – 6 dBi can be attributed to the lack of a ground plane.

220. Utilising the calibrated gain measurements of the helix monopole antennas, the received powers of the copper and NF prototypes were taken at 6 separation distances. All measurements were taken where both the SRR prototype antennas and helix monopole antennas were oriented to the same polarisation. The Antenna Gain results, including cable losses, maximum absorption efficiency, and multipath reduction calculations are contained below in Figures (29 – 31)

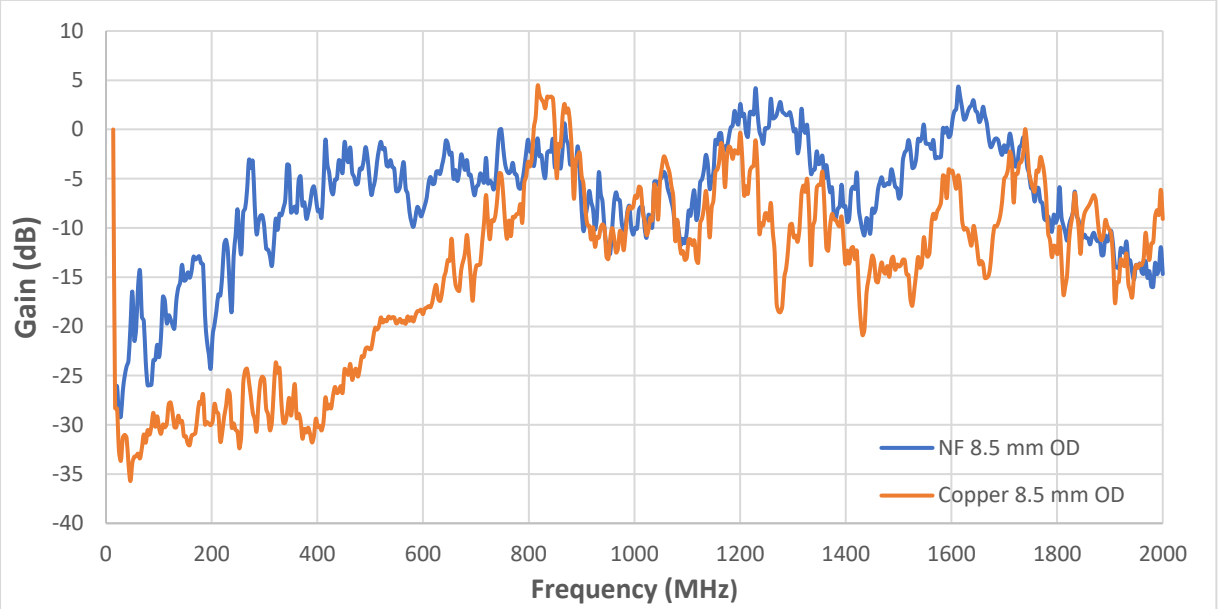

221. *Figure (29): Frequency vs Gain plot for the copper and CNT SRR prototypes.*

222. Both prototypes show very low gains at frequencies below 200 MHz. The lowest prominent gain shown by the NF prototype is at 270 MHz with a gain of -3.1 dBi. The lowest frequency prominent gain for the copper prototype is seen at 733 MHz with a gain of -0.5 dBi. The most significant gain is seen from the copper prototype at 809 MHz, with a gain of 7.5 dBi, however, this frequency corresponds to the mobile phone frequency of the author (Three, at 800 MHz, band 20). As such this reading may or may not be accurate. The NF prototype shows a higher gain on average in comparison with the copper prototype.

223. Figures 30 and 31 below contain the maximum absorption frequencies and gains of the copper and NF prototypes. These are shown to determine any relationship between the two types of measurements.

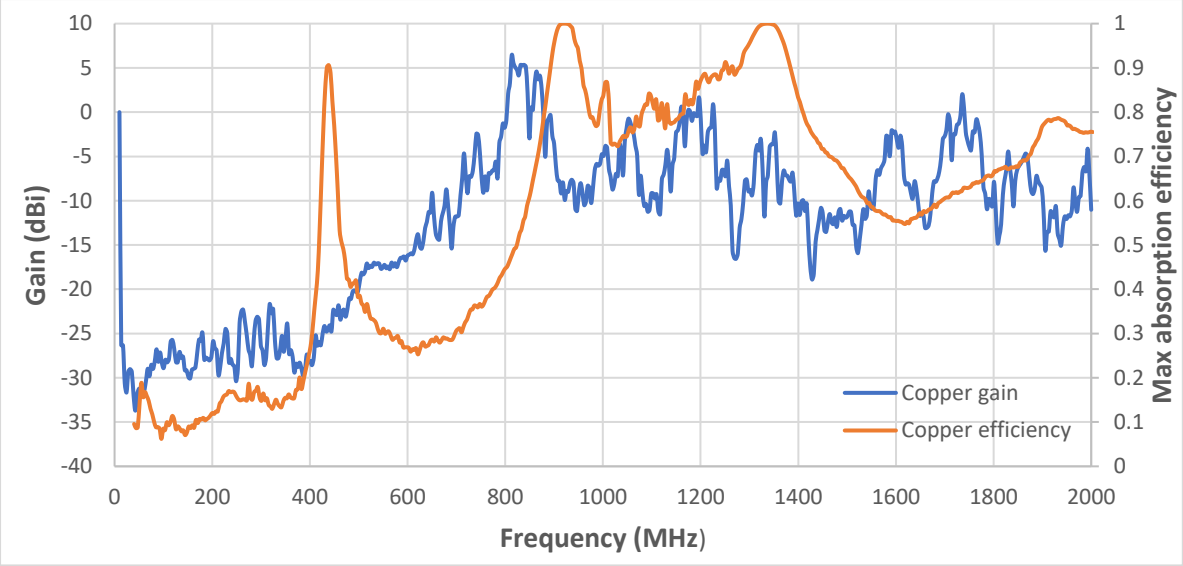

224. *Figure (30): Copper prototype gain & maximum absorption efficiency vs frequency.*

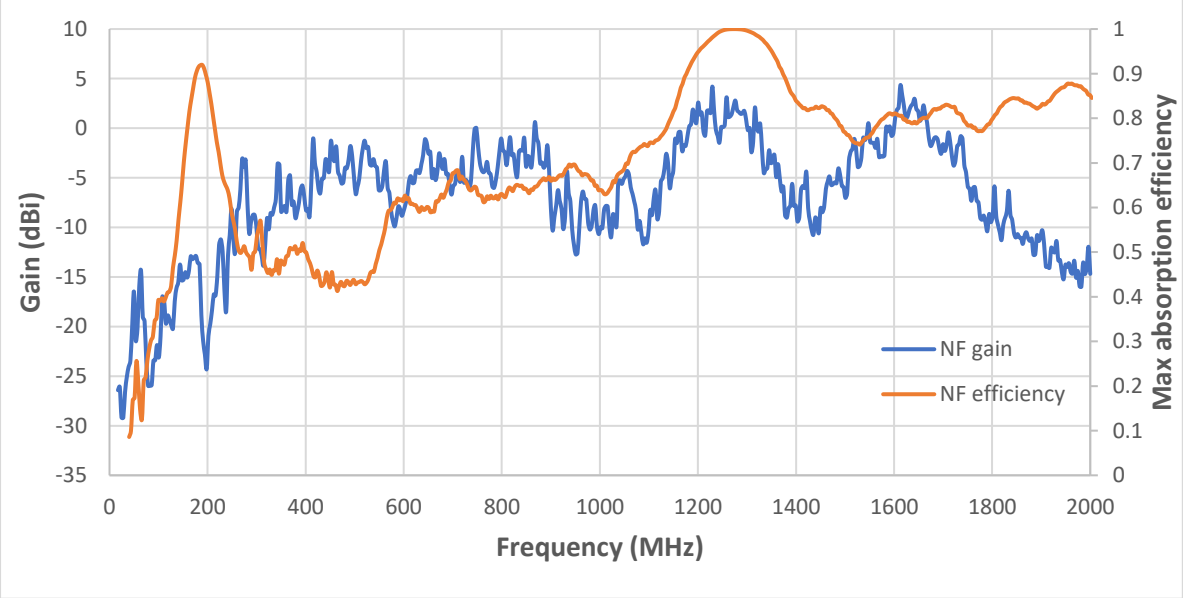

225. *Figure (31): NF prototype gain & maximum absorption efficiency vs frequency.*

226. From the figures above, there doesn't seem to be an immediate relationship between the individual maximum absorption efficiencies and the gains of each prototype measured at the lower frequencies.

227. The gains of each prototype are calculated from the Friis equation (see Appendix 3), and the Friis equation is dependent on the knowledge of the power radiated from any transmitting antenna, the gains here are calculated without knowledge of the power losses inherent to the prototypes. The assumption made for the calculations is as follows;

$$P_t = (P_{sg} - l_c)\, l_p\, M_{ae}$$

228. *Equation (13): Transmit power from prototype antennas, where P_t is the transmitted power (dBm), P_{sg} is the power transmitted from the signal generator (dBm), l_c are the cable losses (attenuation) between the signal generator and the prototype (dB). l_p are the losses*

inherent to the prototype such as ohmic losses, which if known, will be a figure between 0 and 1. M_{ae} is the maximum absorption efficiency, which is a figure between 0 and 1.

229. Equation 13 states the initial power produced at the signal generator, gets reduced initially in the cable between the signal generator and the antenna. Secondly a further reduction will be via any internal losses inherent to the antenna, and finally a certain amount of power will be reflected back to the signal generator due to the capability of the antenna to absorb powers as a function of signal frequency.

230. Likewise, for the power received at the helix monopole;

$$P_r = (P_{rs} + l_c)\, l_p\, M_{ae}$$

231. *Equation (14): Transmit power from prototype antennas, where P_{rs} is the power received at the spectrum analyser (dBm)*

232. Related to equation 13, equation 14 indicates the power received from the receiving antenna into the spectrum analyser will get reduced by cable losses between the receiving antenna and the spectrum analyser. Further losses will likely be incurred again by any internal power losses in the antenna, and once again a certain amount of power will not be absorbed by the antenna (to transmit to the spectrum analyser) as a function of signal frequency.

233. These radiated powers for all gain measurements are calculated using equation 15, where l_p is set to 1 (i.e. no losses inherent to the prototype are factored into the calculation). These internal losses are likely to reduce the amount of energy transmitted from the prototypes. As accurate knowledge of the powers transmitted is required for gain determination (from the Friis equation (equation 22)) it is likely that the gain measurements are higher than reported.

234. How then do the prototypes created for this dissertation compare with the standard SRR configuration as seen in the published literature? As we do not have any gain measurements from the standard SRR configuration to compare against the prototype gain measurements, the return loss results ($S_{(1,1)}$) of the standard SRR will be compared against the copper and SRR prototypes.

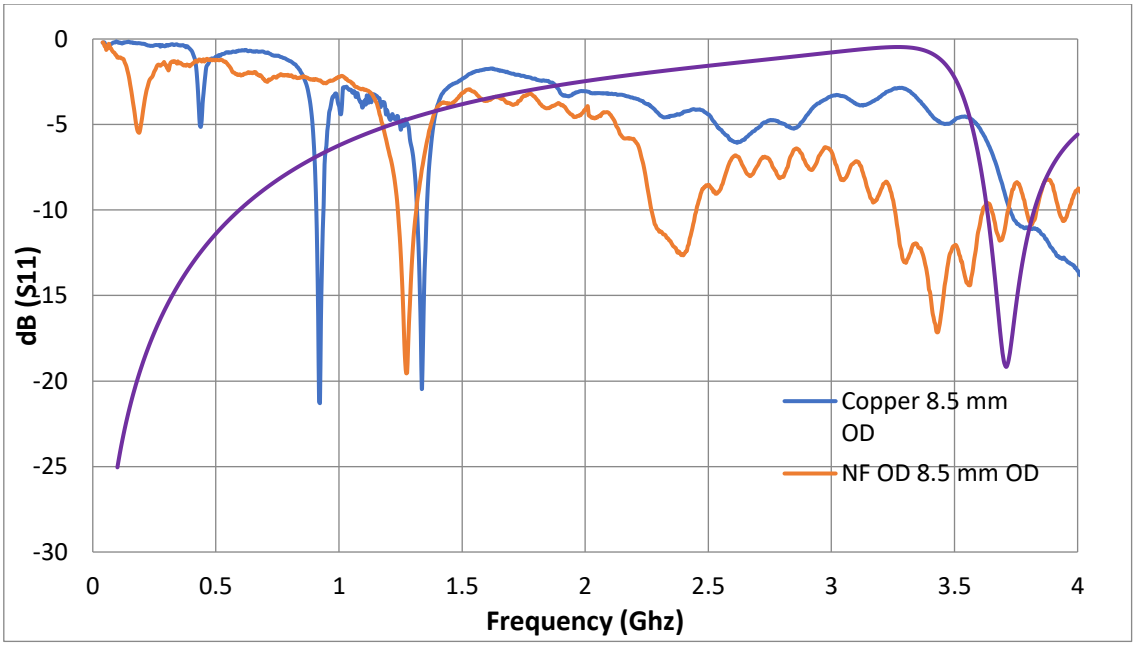

235. *Figure (32): The measured return loss ($S_{(1,1)}$) for the 8.5 mm OD copper and NF prototype, and the simulated return loss for the standard configuration SRR.*

236. As seen in chapter 2, the simulated return loss results of the standard configuration SRR are somewhat inaccurate (≈ 100 MHz) in comparison with the published figures. We can however see a clear difference in the lowest return loss frequencies of the standard configuration SRR and the two prototypes. Please note, the large dip in the sub 1 GHz range in the simulated standard configuration data is an artefact of the simulation software, rather than a low return loss. The lowest return loss of the standard SRR is seen to be at 3.6 GHz while, as seen from the figure above, the lowest NF prototype return loss is seen at 185 MHz, and the lowest copper prototype return loss is seen at 438 MHz. The lowest return losses are seen to be at – 19 dB for the standard SRR compared with ≈ -5 dB for both prototypes. While this may indicate the standard configuration SRR is more efficient at its lower frequencies compared with the two prototypes, as noted above, sub 1 GHz readings for the standard SRR configuration are not available due to the previously mentioned artefact. What we can see however, are secondary and even tertiary return loss frequencies created by the NF and copper prototypes, which are still at frequencies significantly lower than 3.6 GHz, and with return loss values comparable to the standard SRR return loss.

237. Stepping away from split ring resonators, how then do the prototypes compare against standard antennas, such as commonly used ½ λ dipoles? Unfortunately time constraints prevented the physical gain measurements for a ½ λ dipole, however, ½ λ dipoles have gains theoretically equal to 2.15 dBi [59]. Both the copper and NF prototypes have gains equal to 2.15 dBi at approximately 1.2 GHz. At this frequency an equivalent ½ λ dipole will have a length of ≈12.5 cm ±1 cm, as such if we take the largest width of each prototype (1 cm), at a frequency of 1.2 GHz each prototype will show the same performance of an equivalent ½ λ dipole, at ≈1/12th of the size.

Chapter 3: Discussion, Conclusion & Recommendations

239. Discussion & Recommendations for future work.

240. Following the analysis of the results presented in chapter 2, there are certain areas of concern identified by the author and, similarly, other areas of potential improvement and recommendations for future work which will be discussed in this section.

241. Of primary concern regarding the results presented by the NF prototypes are the tails used to connect the outer NF ring to the input coaxial cable. There are two tails, each of approximately 50 mm in length. These tails are connected to the inner core and outer sheath of the coaxial cable. The inner core and outer sheath of the coaxial cable are exposed (outside of the confine of the coaxial cable) for approximately 20 mm. The tails and exposed coaxial components, separate from the fibre attached to the ferrite substrate, will potentially act to affect the results of the testing on the NF by artificially increasing the antenna size. While the tails and exposed coaxial components are oriented at 90^{o} to the receiving helix monopole antenna, (with the tails forming the body of a T shape, and the helix monopole forming the arms) they may be potentially radiating alongside the main component of the prototype. However, it may be that any radiation emitted by the tails and coaxial components is both in the wrong polarisation and primarily directed away from the receiving helix monopole antenna. In addition, the extra path length of the external ring due to the increased fibre and coaxial component length may provide a larger surface area in which to absorb or emit radiation. In contrast, the increased volume of CNT fibre may reduce the efficient operating frequencies (and gains) of the NF prototypes by providing an increased self-inductance. To determine the effects of these tails and exposed coaxial components on the overall performance of any future NF prototypes, any future work should compare the gains and return losses of prototypes with and without tails.

242. The return loss results, as seen in the dissertation, provide the frequencies and bandwidths at which the prototypes absorb the maximum amount of power. A percentage of this power may be lost by interference from the substrate, impedance mismatching, or general ohmic losses. These internal losses are likely to reduce the electrical efficiency of the prototypes across a wide range of frequencies. As a consequence, the calculation for the gain measurements (the Friis equation) requires knowledge of the powers transmitted, the actual powers transmitted from the prototypes are likely to be lower than calculated. The gain measurements are therefore likely to be higher than reported.

243. Related to the above point, and in respect to the issues seen with multipath propagation especially at low frequencies. As the prototypes show very efficient power absorptions at low frequencies, they might be used as compact narrowband bandpass filters, in addition they may also provide narrowband augmentation to the higher frequency Radar Absorbent Material (RAM) utilised in anechoic chambers.

244. . The Raman spectroscopy performed as part of the dissertation do not allow us to determine the length of the nanotubes in the CNT fibre, however, this technique enabled the determination of a range of CNT diameters and, from this, we can assume that there are a range of CNT lengths. None of the CNTs are likely to span the entire length of the fibre. While this may provide some extra capacitance within the fibre (in the volumes between the nanotubes), it is likely that the gaps between nanotubes provides a significant impedance to electron flow, thereby reducing the overall electrical conductivity. Further to this, as we have no indication of the orientation of the nanotubes throughout the fibre, it is likely that the packing density is not as dense as it could be and, as such, there will be a range of gap sizes between the nanotubes, further reducing the electrical conductivity. Fibres comprising fewer CNTs, with lengths comparable to the largest ring circumference,

should allow a greater packing density, a reduced cross-sectional area, enabling a greater self-inductance of the overall fibre and, due to the lack or reduction of any discontinuities in the lattice of individual CNTs, should allow significantly increased electrical conductivities.

245. As the design improvements applied to the prototypes are not seen in the simulations performed to predict the behaviour of the prototypes, a discussion to determine any further optimisation was sought from modelling experts at QinetiQ (the company sponsor of the author). A summary of the potential optimisations include using discrete frequency sweeps at select frequency ranges, in addition to the interpolating sweeps. The interpolating sweeps in the simulations significantly cut down the time required for each simulation, however discrete sweeps will tend to give more accurate results. The lumped port, attached to the outside of the tails in each prototype model, may be best attached to the inside of the tails to permit easier/more-reliable de-embedding. A more accurate model should include the coaxial cable as seen in the real-world testing. Coaxial cables provide unbalanced feeds, while the feeds utilised in the simulation provide a balanced feed. Any unbalanced feed attached to an antenna will enable power reflections back towards the feed point, thereby potentially altering its return losses. This has particular relevance to both the simulation and the real-world performance testing, as a balanced feed may affect the electrical efficiency of the prototypes.

246. Recommendations

247. During prototype testing, both prototypes were oriented in the same direction with the feed point in each prototype (the gap in the outer ring) placed facing away from the receiving helix monopole antenna. Readings in a full 360^{o} in both azimuth and elevation around each prototype were not taken, and it may be that a larger amount of power was transmitted from each prototype at angles. Any future work should therefore take measurements at as many angles as possible.

248. In order to both obtain more accurate gain measurements and any internal electrical losses inherent to any prototypes, future work on these prototypes, and any further electrically small antennas, should employ the Wheeler cap [53] or other equivalent methods.

249. The low frequency performance of the NF prototype, and indeed the electrical conductivity is highly dependent on the geometry on the CNT fibre. This is dependent on the diameter, length and packing density of the nanotubes inside the fibre, techniques such as scanning electron microscopy should be used in addition to Raman spectroscopy at a greater range of wavelengths, to get accurate measurements of the surface geometry of the fibre and, if possible, the length of the nanotubes.

250. All prototypes utilised in this dissertation have been made by hand, and the split and gap distances have effectively been limited to approximately 1 mm. A more accurate manufacturing processes, where these distances are reduced should enable a lowering of efficient antenna frequencies. The laser reduction of graphene oxide, as per the method currently employed for graphene based super-capacitors [54], could be used effectively and cheaply in order to print SRR designs with split and gap distances far smaller than employed in the prototypes created for this dissertation. Likewise, as these super-capacitors rely on very high surface areas, and the energy storage is contained within the electric field, rather than in a chemical solution, this technique would appear to be ideally suited for quick and accurate prototyping and possible mass production of these types of antennas. In addition, in order to obtain a balanced electrical feed to any future prototype, especially when utilising coaxial cables, it is recommended a balun is added.

251. Conclusion

252. The primary purpose of this dissertation has been to determine whether COTS CNT fibre is at a materials readiness level in which it can be used as the conducting element in an individual split ring resonator. Further, should this objective have been met, does the CNT SRR give any benefit in comparison with equivalent sized SRR made from copper? Design improvements including the addition of a substrate with material properties which enable enhancement of the capacitance and inductance inherent to split ring resonators, alongside the favourable geometry of the CNT fibre have enabled both objectives to be met. In addition, the substrate modification has been shown to enable lower frequency radiation from copper split ring resonators. The recommendations suggested above should hopefully further provide more substantial evidence as to whether both of these objectives have been met.

253. It is expected that further improvement in the electrical conductivity, and an increase in the length of the carbon nanotubes utilised in any future CNT fibre will significantly increase the ability of the CNT fibres to be used for RF application. In addition, the efficient absorption of incident RF at low frequencies (in relation to the size of the antennas) may enable improved capabilities in the design of RF test chambers.

254. The modelling employed to support prototype development and predict the operating frequencies of the prototypes produced results that were significantly different than those obtained during real world testing. More accurate materials properties, alongside substantial refinement of the simulation setup should go some way to reducing the inaccuracies.

This page intentionally left blank

APPENDIX 1 – The Resonant Frequency Of An SRR.

255. The appendix contains the physics and mathematics drawn from the literature reviewed pertaining primarily to the resonant frequency of the standard split ring resonator configuration.

256. The calculations provided by [1] show the ability to calculate the capacitance between a unit length of parallel sections of the magnetic strips, providing the following conditions are met

$$r >> c, \quad r >> d$$

$$\ln\frac{c}{d} >> \pi$$

257. *Where r is the outer ring radius, c is the inner and outer ring split widths, and d is the inner and outer ring gap widths*

258. The capacitance between a unit length of two parallel sections of the metallic strips is then given as;

$$C_1 = \frac{\varepsilon_0}{\pi}\ln\frac{2c}{d} = \frac{1}{\pi\mu_0 c_0^2}\ln\frac{2c}{d}$$

259. *Equation (15): The capacitance between two parallel sections of metallic strips in a split ring resonator*

260. Following this, the equation for calculating the effective magnetic permeability (below) is given by the authors on the assumption that the split ring structures shown are stacked, one above the other with the rings being sufficiently close together that any magnetic lines of force are essentially the same as those in a continuous cylinder.

$$\mu_{eff} = 1 - \frac{\frac{\pi r^2}{a^2}}{1 + \frac{2\ell\sigma_1}{\omega r\mu_0} i - \frac{3\ell}{\pi^2\mu_0\omega^2 C_1 r^3}} = 1 - \frac{\frac{\pi r^2}{a^2}}{1 + \frac{2\ell\sigma_1}{\omega r\mu_0} i - \frac{3\ell c_0^2}{\pi\omega^2 \ln\frac{2c}{d} r^3}}$$

261. *Equation (16): The effective magnetic permeability of an SRR, where σ1* is the resistance per unit *length of the sheets measured around the circumference, d is the ring separation distance (the gap distance), a is the effective surface area of outer ring, and l is the distance between the stacked rings.*

262. Further, the authors give the resonant frequency of a stacked SRR array.

$$\omega_0^2 = \frac{3\ell c_0^2}{\pi \ln\frac{2c}{d} r^3}$$

263. *Equation (17): The resonant frequency of a stacked SRR array.*

264. Analysis of the electromagnetic properties of individual SRRs in [55] indicate that an SRR will behave as a LC with a resonance given by a modification of the standard LC resonance equation shown below. The topology and an equivalent circuit diagram for an individual SRR from [56] are shown below;

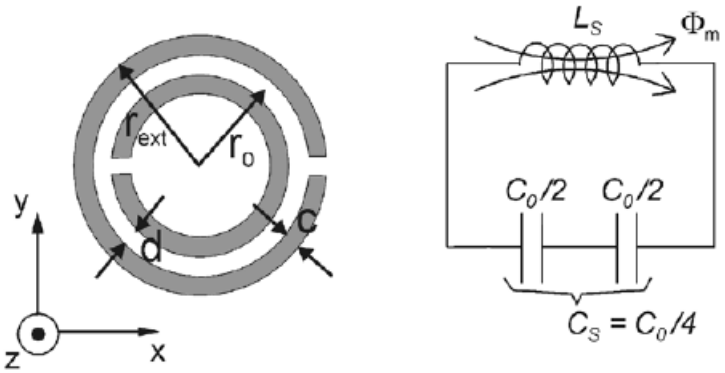

265. *Figure (33): The topology and associated circuit diagram for an individual SRR, where C_0 is the total capacitance between the rings.[56]*

266. The total capacitance between the inner and outer ring is then given by;

$$C_0 = 2*\pi*r_0*C_{ul}$$

267. *Equation (18): The total capacitance between the inner and outer ring of an SRR, where r_0 is the average radius of the SRR, and C_{ul} is the capacitance per unit length*

268. The resonance frequency is then given by the authors to be;

$$F_0 = (L_s C_s)^{-1/2}/2\pi$$

269. *Equation (19): The modified resonance frequency of an individual SRR given by [56], where C_s is the capacitance of the upper and lower halves of the SRR (when oriented as the topology shown above). The inductance (L_s) is therefore approximated by a single ring of radius r_0, and width c.*

270. *Note: The analysis in this Appendix has not been used to calculate the theoretical resonant frequency of the SRR prototypes studied for this thesis due to the unknown surface geometry, and self-capacitance/self-inductance of the CNT NF SRRs.*

APPENDIX 2 – The Standard SRR Configuration Simulation Setup

271. Contained within this section is the configuration of the standard SRR and an explanation of the simulation setup properties utilised in numerous papers reviewed for this dissertation.

272. As discussed in [57], and seemingly utilised in numerous papers, the technique below simulates the expected behaviour of an individual SRR in an infinite array, however should only be used for reference when dealing with individual SRR elements.

273. In HFSS, the models are placed in a simulated waveguide of dimensions 8 mm x 8 mm x 8 mm. The bottom floor of the waveguide is situated 2.4mm below the underneath of the substrate, and the ceiling is situated 3.97 mm above the surface of the copper ring. The ceiling and floor of the waveguide have perfectly matched H boundaries (magnetic field boundaries) applied to provide boundary matching conditions for the incident wave. Internal sides A and B (indicated below) have perfectly matched E boundaries (electrical boundaries) applied.

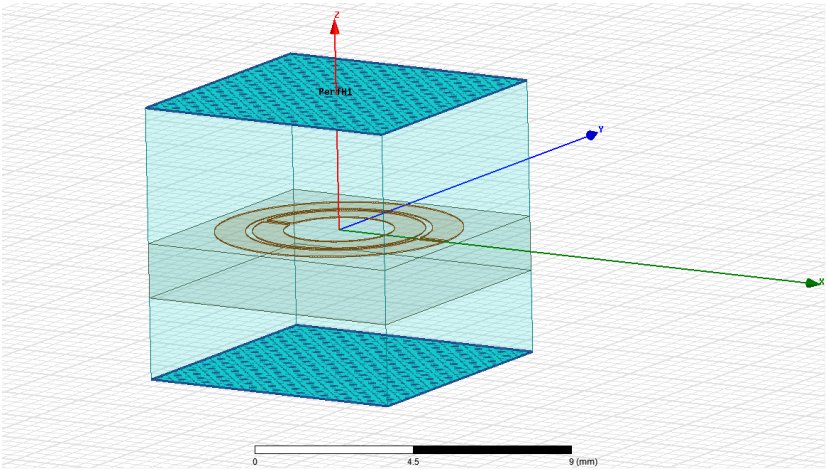

Figure (34): The matched H boundaries

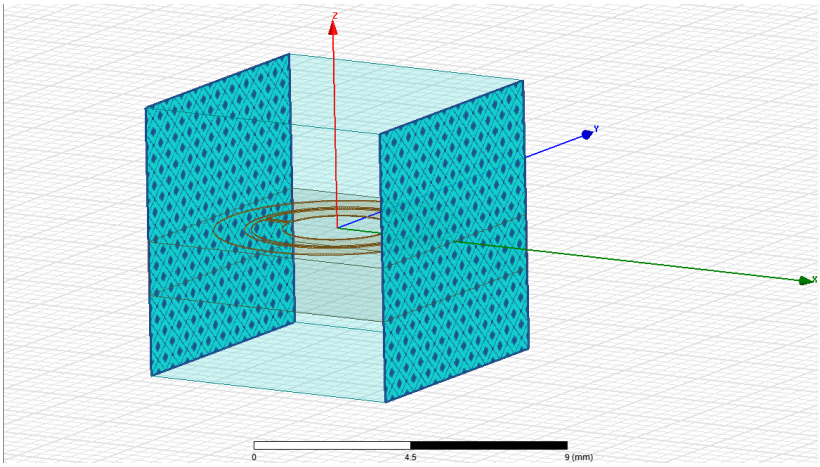

Figure (35): The matched E boundaries

274. Two lumped ports are applied on the other two layers (port 1 and 2). Lumped ports are simple port inputs that excite voltages and associated currents at the specified locations. Integration lines are applied to the lumped ports. The integration lines determine the polarisation of the produced E field, and, by default, the produced H field as well.

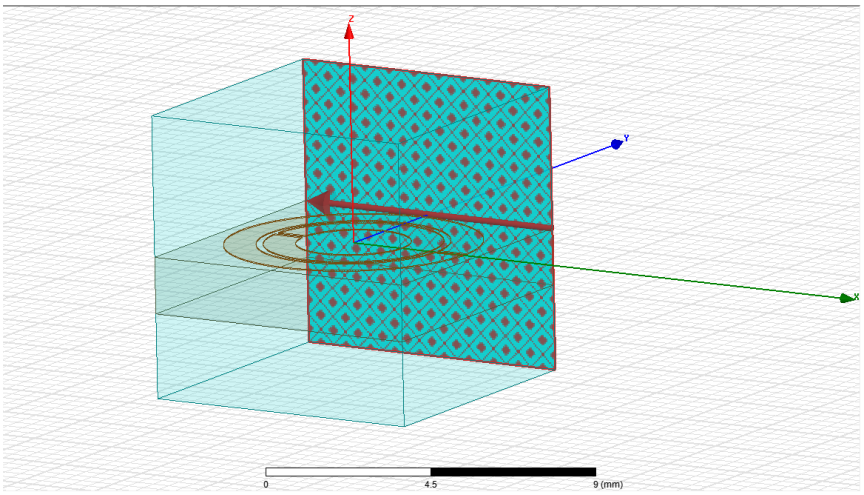

275. *Figure (36): Port one (with integration line displayed*)

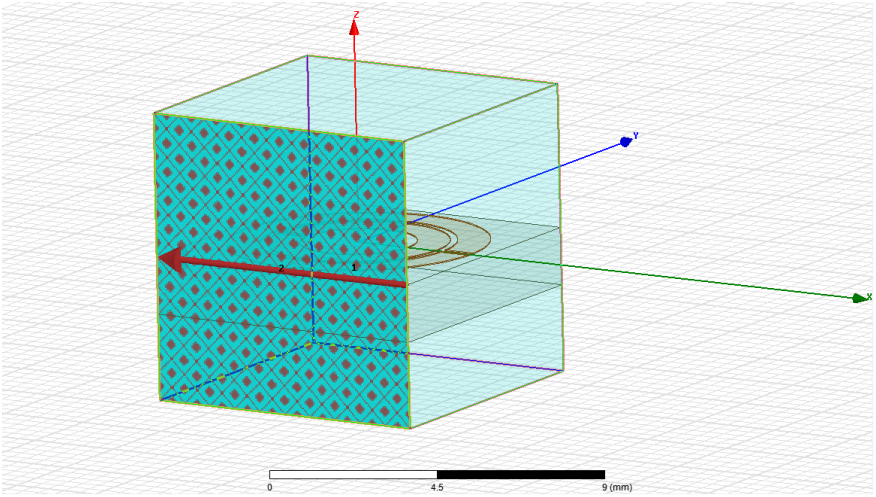

276. *Figure (37): Port two (with integration line displayed)*

277. Results output from the simulations include return losses ($S_{1,1}$) plots), and transmission losses ($S_{1,2}$) plots

APPENDIX 3 – Helix Monopole Gain Calibration Procedure.

278. As there were no suitable gain calibrated antennas covering the entirety of the frequency range available at the test facility, two identical off the shelf antennas, (specified as helix monopoles throughout this dissertation (see figure 25) were initially calibrated using the two-antenna method. This calibration was then subsequently verified in the 20 MHz-2 GHz range against an antenna with a known gain.

279. The calibration method is outlined below;

280. Using the two-antenna method, the gain of two identical antennas can be determined from a derivation of the of the Friis transmission formula. Providing we know the transmission power from one antenna, the receive power at the other and the separation distances between the two, we can solve the Friis equation (in log form);

$$P_r = G_t + G_r + P_t + 20\,log_{10}\left(\frac{\lambda}{4\pi R}\right)$$

281. *Equation (20): The Friis equation.*

282. Solving for two different antennas;

$$G_t + G_r = 20\,log_{10}\left(\frac{4\pi R}{\lambda}\right) + 10\,log_{10}\left(\frac{P_r}{P_t}\right)$$

283. *Equation (21): The Friis equation solved for the gain of two different antennas.*

284. While for two identical antennas;

$$G_t = G_r = \frac{1}{2}[20\,log_{10}\left(\frac{4\pi R}{\lambda}\right) + 10\,log_{10}\left(\frac{P_r}{P_t}\right)]$$

285. *Equation (22): The Friis equation solved for the gain of two different antennas.*

286. *Where in all variations of the Friis equation, Gt and Gr are the transmit antenna gain, and receive antenna gain respectively (both in dBm). R is the separation distance (m), lambda is the wavelength of the radiation (m), and Pr and Pt are the powers received and transmitted from their respective antennas (both in dBm).*

287. Readings were taken from the receive helix monopole at several separation distances (1.69 m, 2.07 m, 2.45 m, 3.13 m, 3.79 m, and 4.44 m). Readings were taken at a range of distances due to concerns about multipath. Readings were taken between 10 MHz and 2 GHz. The transmit power was set to 10 dBm (0.01 Watts). The receive helix monopole was fed into an Anritsu MS2724B spectrum analyser, and the transmitted power was fed into the transmit monopole from a HP83732B signal generator. Both antennas were situated at 1.5 meters from the ground during all readings, and oriented in the same direction.

288. The data analysis included gain measurements (from the Friis equation) calculated at all separation distances, and all gain measurements averaged, in order to attempt to reduce any influence of multipath propagation.

289. Further to this, all readings were repeated at the same distances against a Harris AS-48410 quad ridged horn antenna, with a known gain between 1 – 2 GHz. One of the helix monopole antennas was utilised as the transmit antenna, and the Harris horn antenna was utilised as the receive antenna.

290. With the gain of the Harris horn known, the Friis equation was used to verify the gain measurements taken via the two-antenna method. Results are given below (Figure 38). The figure shows the approximate similarities of the two results. Likewise, the results also indicate the poor performance of the horn antenna below 1000 MHz.

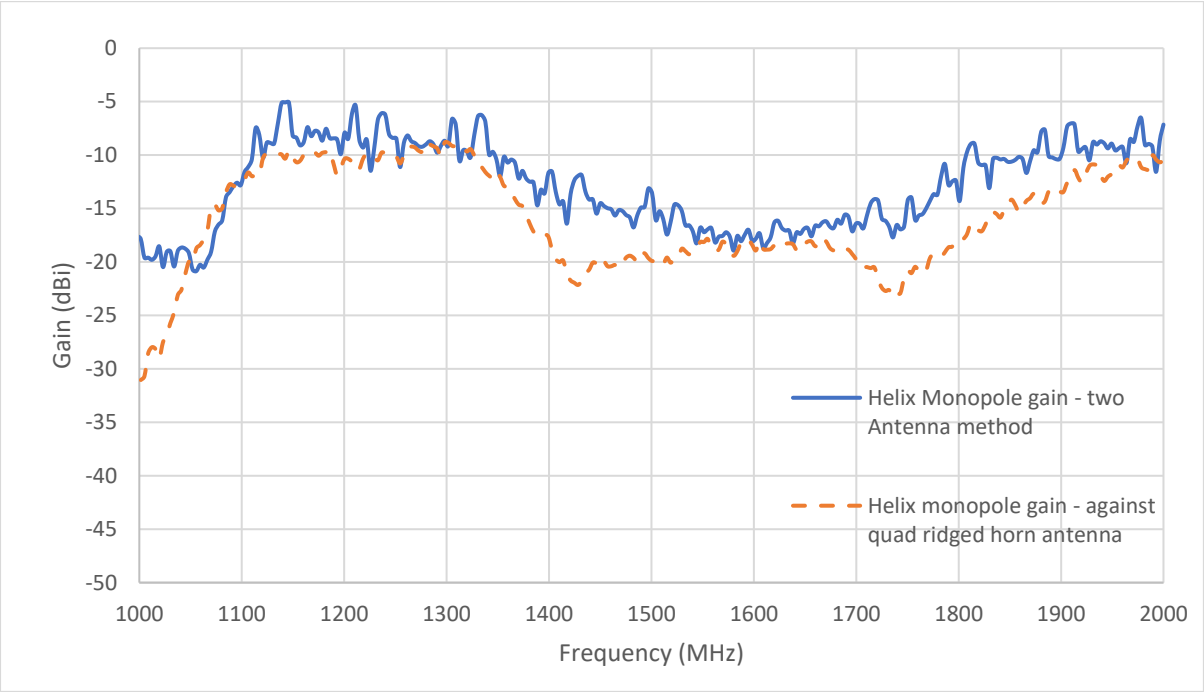

291. *Figure (38): Helix monopole gain measurements. Note: the drop off of the gain measurements against the quad ridged horn near to 1000 MHz showing the poor performance of the horn antenna at this frequency.*

292. ## Experimental testing procedure to determine prototype gain.

293. In much the same way as the gain calibration of the helix monopole antennas, the gain measurements of the 8.5 mm OD copper SRR, and the 8.5 mm OD SRR were taken at a range of separation distances (1.03 m, 1.53 m, 2.25 m, 2.8 m, 4.2 m, and 4.44 m).

294. Both prototypes were oriented face-up (with the rings pointing towards the ceiling of the chamber), and the Helix monopole was oriented 90^{o} to its normal position, i.e. oriented parallel to the ground.

295. The helix monopole antenna was used as the receive antenna for testing against each prototype, and the same spectrum analyser and signal generator were used. The broadcast power was again set to 10 dBm (0.01 Watts).

296. The gains were determined from each separation distance individually, and all gains were averaged in order to reduce any interference effects from multipath propagation (defined below).

297. ## Data analysis

298. Accurate gain measurements using the Friis equation are dependent on knowledge of the powers radiated by the transmit antenna, and the powers received by the receive antenna. Cable losses and antenna absorption efficiencies both affect the powers into and

transmitted from each antenna. Cable losses will tend to attenuate any signals, and are generally measured in dB as a function of frequency. Antenna absorption efficiencies are inherent to each antenna.

299. The cable losses were performed in situ at both the transmission and receive ends of the test chamber. A spectrum analyser was connected to one end of each cable, and the other end was connected to a HP83732B signal generator. The signal generator was swept through a full 1.99 GHz range (10 MHz to 2 GHz), at a power output of 10 dBm (0.01 Watts). The difference in received powers at the spectrum analyser and transmitted powers (10 dBm) is the cable loss. Further to this, the helix monopole antennas are attached to a 2.4 mm diameter coaxial cable of 2.5 m length. Results below.

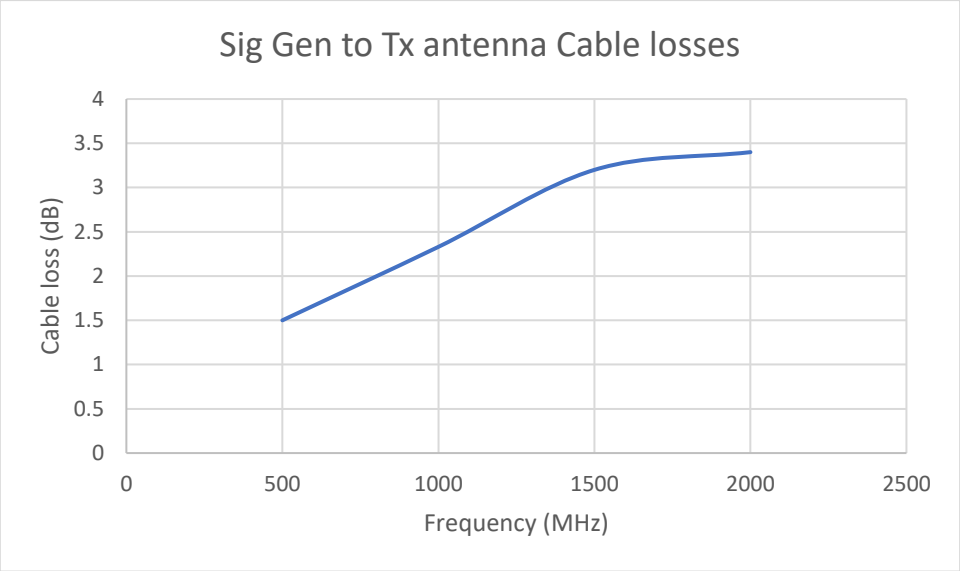

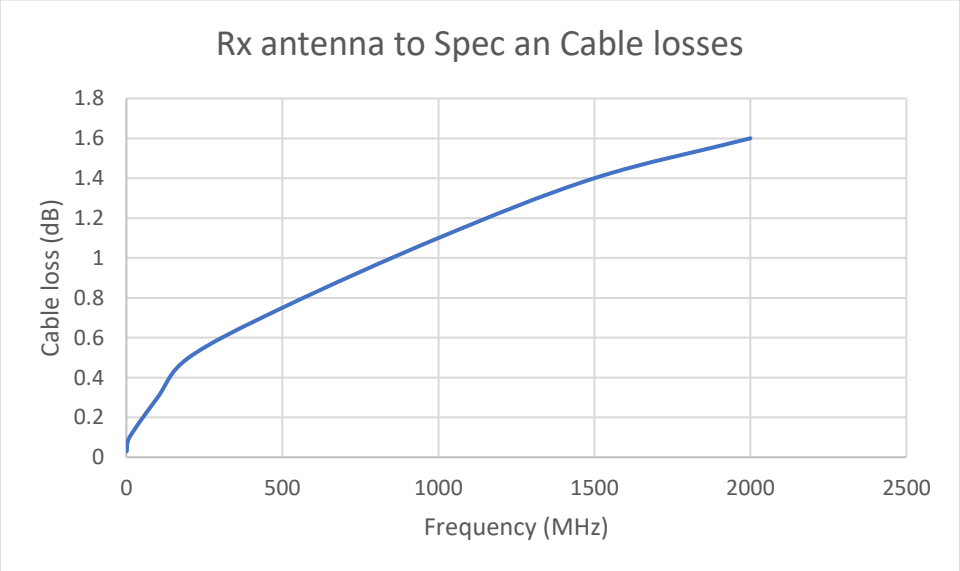

300. *Figures (39) & (40): Measured cable losses*.

301. Near field calculations

302. There is the potential for a receive antenna at close range to an antenna radiating at low frequency to undergo undue effects due to near field interference. Two distances are of concern, the reactive near field and the Fresnel region, or the radiating near field region. In

the reactive near field region the E and H fields are potentially out of phase by 90 degrees to each other. In the Fresnel region the shape of the radiation pattern varies significantly with distance. In both near field regions, depending on the orientation of both the receive and transmit antennas with respect to each other, near field effects may produce readings that are unlikely to be representative of readings in the far field. While in some instances near field effects may be advantageous (see near field communications), the prototype antennas created for this dissertation are primarily intended for use in communications, and hence radiate predominantly/receive in the far field region.

303. The calculations for determining the near field distances are detailed as below;

304. Reactive Near Field [60];

$$R_{NF} \leq 0.62 \times \sqrt{\frac{D^3}{\lambda}}$$

305. *Equation (23): The reactive near field distance.*

306. Radiating Near Field (Fresnel Region) [61]

$$F_R \leq \frac{2D^2}{\lambda}$$

307. *Equation (24): The radiating near field distance, where for both the reactive and radiating near fields, D is defined as the length or thickness of the broadcasting antenna, the helix monopole in this case with a length of 0.2 m.*

308. At the lowest test frequency of 10 MHz, the Reactive near field (R_{NF}) is calculated as $\leq$0.022 m, and the radiating near field (F_R) is calculated as $\leq$0.002 m.

309. As such, as the nearest antenna separation distance in the prototype testing is defined 1.03 m (see appendix 3), there shouldn't be any near field interference effects.

References

1. Pendry J, Holden A, Robbins D, Stewart W. Magnetism from conductors and enhanced nonlinear phenomena. IEEE Transactions on Microwave Theory and Techniques. 1999;47(11):2075-2084.

2. Iijima S, Ichihashi T. Single-shell carbon nanotubes of 1-nm diameter. Nature. 1993;363(6430):603-605.

3. Veselago V. The electrodynamics of substances with simultaneously negative values of ε and μ. Soviet Physics Uspekhi. 1968;10(4):509-514.

4. Wheeler H. Fundamental limitations of small antennas. Proceedings of the IRE. 1947;35(12):1479-1484.

5. Chu L. Physical Limitations of omni-directional antennas. Journal of Applied Physics. 1948;19(12):1163-1175.

6. Alici K, Ozbay E. Electrically small split ring resonator antennas. Journal of Applied Physics. 2007;101(8):083104.

7. Aydin K, Bulu I, Guven K, Kafesaki M, Soukoulis C, Ozbay E. Investigation of magnetic resonances for different split-ring resonator parameters and designs. New Journal of Physics. 2005;7:168-168.

8. Katsarakis N, Koschny T, Kafesaki M, Economou E, Soukoulis C. Electric coupling to the magnetic resonance of split ring resonators. Applied Physics Letters. 2004;84(15):2943-2945.

9. SAUVIAC B, SIMOVSKI C, TRETYAKOV S. Double Split-ring resonators: Analytical modelling and numerical simulations. Electromagnetics. 2004;24(5):317-338.

10. Shamonin M, Shamonina E, Kalinin V, Solymar L. Properties of a metamaterial element: Analytical solutions and numerical simulations for a singly split double ring. Journal of Applied Physics. 2004;95(7):3778-3784.

11. Ekmekci E, Turhan-Sayan G. comparitive investigation of resonance characteristics and electrical size of the double sided SRR, BC-SRR and conventional SRR type metamaterials for varying substrate parameters. Progress In Electromagnetics Research B. 2009;12:35-62.

12. Baena J, Marqués R, Medina F, Martel J. Artificial magnetic metamaterial design by using spiral resonators. Physical Review B. 2004;69(1).

13. Snyder J, Grover F. Inductance calculations working formulas and tables. Mathematics of Computation. 1964;18(85):164.

14. Kroto H, Heath J, O'Brien S, Curl R, Smalley R. C60: Buckminsterfullerene. Nature. 1985;318(6042):162-163.

15. Balkanski M. Physical Properties of Carbon Nanotubes, Edited by R. Saito, G. Dresselhaus and M.S. Dresselhaus, Imperial College Press, London, 1998. Materials Science and Engineering: B. 2000;76(3):241-242.

16. Iijima S. Helical microtubules of graphitic carbon. Nature. 1991;354(6348):56-58.

17. Rykov V, Lukyanovich V, Radushkevich L. The natural sorbents of the Far East. Bulletin of the Academy of Sciences of the USSR Division of Chemical Science. 1953;1(3):395-397.

18. Iijima S, Ichihashi T. Single-shell carbon nanotubes of 1-nm diameter. Nature. 1993;363(6430):603-605.

19. Balkanski M. Physical properties of carbon nanotubes, Edited by R. Saito, G. Dresselhaus and M.S. Dresselhaus, Imperial College Press, London, 1998. Materials Science and Engineering: B. 2000;76(3):241-242.

20. Belin T, Epron F. Characterization methods of carbon nanotubes: a review. Materials Science and Engineering: B. 2005;119(2):105-118.

21. Wilder J, Venema L, Rinzler A, Smalley R, Dekker C. Electronic structure of atomically resolved carbon nanotubes. Nature. 1998;391(6662):59-62.

22. Murakami Y, Miyauchi Y, Chiashi S, Maruyama S. Direct synthesis of high-quality single-walled carbon nanotubes on silicon and quartz substrates. Chemical Physics Letters. 2003;377(1-2):49-54.

23. Belin T, Epron F. Characterization methods of carbon nanotubes: a review. Materials Science and Engineering: B. 2005;119(2):105-118.

24. Ouyang M. Energy Gaps in "Metallic" Single-Walled Carbon Nanotubes. Science. 2001;292(5517):702-705.

25. An Introduction to graphene and carbon nanotubes by John Edward Proctor, Daniel Alfonso Melendrez Armada, and Aravind Vijayaraghavan. MRS Bulletin. 2018;43(2):148-149.

26. Pletikosić I, Kralj M, Pervan P, Brako R, Coraux J, N'Diaye A et al. Dirac Cones and Minigaps for Graphene on Ir(111). Physical Review Letters. 2009;102(5).

27. Burdick G. Energy band structure of copper. Physical Review. 1963;129(1):138-150.

28. Kollár J. Calculation of the Fermi velocity in tungsten. Solid State Communications. 1978;27(12):1313-1316.

29. Dresselhaus M, Dresselhaus G, Saito R, Jorio A. Raman spectroscopy of carbon nanotubes. Physics Reports. 2005;409(2):47-99.

30. Kataura H, Kumazawa Y, Maniwa Y, Umezu I, Suzuki S, Ohtsuka Y et al. Optical properties of single-wall carbon nanotubes. Synthetic Metals. 1999;103(1-3):2555-2558.

31. Grace T, Yu L, Gibson C, Tune D, Alturaif H, Al Othman Z et al. Investigating the Effect of Carbon Nanotube Diameter and Wall Number in Carbon Nanotube/Silicon Heterojunction Solar Cells. Nanomaterials. 2016;6(3):52.

32. Hároz E, Duque J, Rice W, Densmore C, Kono J, Doorn S. Resonant Raman spectroscopy of armchair carbon nanotubes: Absence of broadG−feature. Physical Review B. 2011;84(12).

33. Vigolo B. Macroscopic Fibers and Ribbons of oriented carbon nanotubes. Science. 2000;290(5495):1331-1334.

34. Vigolo B, Poulin P, Lucas M, Launois P, Bernier P. Improved structure and properties of single-wall carbon nanotube spun fibers. Applied Physics Letters. 2002;81(7):1210-1212.

35. Ericson L. Macroscopic, Neat, Single-walled carbon nanotube fibers. Science. 2004;305(5689):1447-1450.

36. Zhang M. Multifunctional carbon nanotube yarns by downsizing an ancient technology. Science. 2004;306(5700):1358-1361.

37. Liu K, Sun Y, Lin X, Zhou R, Wang J, Fan S et al. Scratch-resistant, highly conductive, and high-strength carbon nanotube-based composite yarns. ACS Nano. 2010;4(10):5827-5834.

38. Li Y. Direct spinning of carbon Nanotube fibers from chemical vapor deposition synthesis. Science. 2004;304(5668):276-278.

39. Motta M, Moisala A, Kinloch I, Windle A. High performance fibres from 'dog bone' carbon nanotubes. Advanced Materials. 2007;19(21):3721-3726.

40. Yi Huang, Wen-Yan Yin, Qing Huo Liu. Performance prediction of carbon nanotube bundle dipole antennas. IEEE Transactions on Nanotechnology. 2008;7(3):331-337.

41. Amram Bengio E, Senic D, Taylor L, Tsentalovich D, Chen P, Holloway C et al. High efficiency carbon nanotube thread antennas. Applied Physics Letters. 2017;111(16):163109.

42. Alici K, Ozbay E. Electrically small split ring resonator antennas. Journal of Applied Physics. 2007;101(8):083104.

43. Matula R. Electrical resistivity of copper, gold, palladium, and silver. Journal of Physical and Chemical Reference Data. 1979;8(4):1147-1298.

44. Liu K, Deslippe J, Xiao F, Capaz R, Hong X, Aloni S et al. An atlas of carbon nanotube optical transitions. Nature Nanotechnology. 2012;7(5):325-329.

45. Gao G, Çagin T, Goddard W. Energetics, structure, mechanical and vibrational properties of single-walled carbon nanotubes. Nanotechnology. 1998;9(3):184-191.

46. Huang Y. Radiation efficiency measurements of small antennas. Handbook of Antenna Technologies. 2015;:1-21.

47. Classical Electrodynamics. Von J. D. Jack-son 2. Auflage John Wiley & Sons, Inc., New York/London/Sidney/Toronto (1975), 848 S., $21.95, £ 10.75. Physik in unserer Zeit. 1976;7(4):128-128.

48. Baena J, Bonache J, Martin F, Sillero R, Falcone F, Lopetegi T et al. Equivalent-circuit models for split-ring resonators and complementary split-ring resonators coupled to planar transmission lines. IEEE Transactions on Microwave Theory and Techniques. 2005;53(4):1451-1461.

49. Gao G, Çagin T, Goddard W. Energetics, structure, mechanical and vibrational properties of single-walled carbon nanotubes. Nanotechnology. 1998;9(3):184-191.

50. Gao G, Çagin T, Goddard W. Energetics, structure, mechanical and vibrational properties of single-walled carbon nanotubes. Nanotechnology. 1998;9(3):184-191.

51. Snyder J, Grover F. Inductance calculations working formulas and tables. Mathematics of Computation. 1964;18(85):164.

52. Wyatt D. Introduction to antenna placement and installation. T. M. Macnamara. John Wiley and Sons, The Atrium, Southern Gate, Chichester, West Sussex, UK, PO19 8SQ. 2010. 394pp. Illustrated. £85. ISBN 978-0-470-01981-8. The Aeronautical Journal. 2011;115(1172):650.

53. Moharram M, Kishk A. Unrestricted wideband prediction for antenna radiation efficiency using wheeler caps. IEEE Transactions on Antennas and Propagation. 2016;64(7):2869-2883.

54. Tran T, Choi H, Che C, Sul J, Kim I, Lee S et al. Laser-induced reduction of graphene oxide by intensity-modulated line beam for supercapacitor applications. ACS Applied Materials & Interfaces. 2018;10(46):39777-39784.

55. Marques R, Mesa F, Martel J, Medina F. Comparative analysis of edge- and broadside-coupled split ring resonators for metamaterial design - Theory and experiments. IEEE Transactions on Antennas and Propagation. 2003;51(10):2572-2581.

56. Baena J, Bonache J, Martin F, Sillero R, Falcone F, Lopetegi T et al. Equivalent-circuit models for split-ring resonators and complementary split-ring resonators coupled to planar transmission lines. IEEE Transactions on Microwave Theory and Techniques. 2005;53(4):1451-1461.

57. Weiland T, Schuhmann R, Greegor R, Parazzoli C, Vetter A, Smith D et al. Ab initio numerical simulation of left-handed metamaterials: Comparison of calculations and experiments. Journal of Applied Physics.

58. Using Nanomaterials at Work. Including carbon nanotubes (CNTs) and other bio-persistent high aspect ratio nanomaterials (HARNs), The Health and Safety Executive (England and Wales), HSG272, 2013

59. Weik M.H. (2000) half-wave dipole antenna. In: Computer Science and Communications Dictionary. Springer, Boston, MA

60. Reactive near-field region radiation of planar UWB antennas close to a dispersive tissue model, 2012 Loughborough Antennas & Propagation Conference (LAPC), 12-13 Nov. 2012

61. Fraunhofer and Fresnel Distances: Unified derivation for aperture antennas, IEEE Antennas and Propagation Magazine (Volume: 59, Issue: 4 , Aug. 2017

62. Tight-binding model for carbon nanotubes from ab initio calculations, Journal of Physics Condensed Matter, July 2010

63. Giancoli, Douglas C., Physics, 4th Ed, Prentice Hall, (1995)